Title

Age-dependent regulation of SARS-CoV-2 cell entry genes and cell death programs correlates with COVID-19 severity.

Journal

Science advances, 7(34)

ISSN

2375-2548

Authors

Inde, Zintis
Croker, Ben A
Yapp, Clarence
et al.

Publication Date

2021-08-01

DOI

10.1126/sciadv.abf8609

Peer reviewed

CORONAVIRUS

Age-dependent regulation of SARS-CoV-2 cell entry genes and cell death programs correlates with COVID-19 severity

Zintis Inde[1,2†], Ben A. Croker[3†], Clarence Yapp[2,4], Gaurav N. Joshi[1,2,5], Johan Spetz[1,2], Cameron Fraser[1,2], Xingping Qin[1,2], Le Xu[6], Brian Deskin[1], Elisa Ghelfi[1], Gabrielle Webb[1], Aaron F. Carlin[6], Yanfang Peipei Zhu[3], Sandra L. Leibel[3,7,8], Aaron F. Garretson[6], Alex E. Clark[6], Jason M. Duran[6], Victor Pretorius[9], Laura E. Crotty-Alexander[6], Chendi Li[10], Jamie Casey Lee[3], Chhinder Sodhi[11], David J. Hackam[11], Xin Sun[3], Aaron N. Hata[10,12], Lester Kobzik[1], Jeffrey Miller[1], Jin-Ah Park[1], Douglas Brownfield[1], Hongpeng Jia[11], Kristopher A. Sarosiek[1,2]*

Novel coronavirus disease 2019 (COVID-19) severity is highly variable, with pediatric patients typically experiencing less severe infection than adults and especially the elderly. The basis for this difference is unclear. We find that mRNA and protein expression of angiotensin-converting enzyme 2 (ACE2), the cell entry receptor for the novel severe acute respiratory syndrome coronavirus 2 (SARS-CoV-2) that causes COVID-19, increases with advancing age in distal lung epithelial cells. However, in humans, ACE2 expression exhibits high levels of intra- and interindividual heterogeneity. Further, cells infected with SARS-CoV-2 experience endoplasmic reticulum stress, triggering an unfolded protein response and caspase-mediated apoptosis, a natural host defense system that halts virion production. Apoptosis of infected cells can be selectively induced by treatment with apoptosis-modulating BH3 mimetic drugs. Notably, epithelial cells within young lungs and airways are more primed to undergo apoptosis than those in adults, which may naturally hinder virion production and support milder COVID-19 severity.

INTRODUCTION

The novel coronavirus disease 2019 (COVID-19) pandemic has caused infection of more than 151 million individuals and greater than 3 million deaths globally as of 4 May 2021 (*1*). Disease severity is typically lower in pediatric patients than adults (particularly the elderly), but higher rates of hospitalizations requiring intensive care are observed in infants than in older children (*2*–*4*). The causal agent for COVID-19, the novel severe acute respiratory syndrome coronavirus 2 (SARS-CoV-2), infects host cells through interaction with the cell surface proteins angiotensin-converting enzyme 2 (ACE2) and transmembrane serine protease 2 (TMPRSS2) (*5*). For SARS-CoV-2 infection to occur, the spike protein of a viral particle must bind ACE2 and undergo cleavage by TMPRSS2 to allow the particle to fuse with the host plasma membrane and gain entry into the cell (*5*). In the respiratory system, where this process is known to occur, developmental processes in early life require coordinated regulation of gene expression to ensure proper formation and maturation of airways and alveoli (*6*). It remains unknown how these developmental processes affect ACE2 expression and host cell responses to SARS-CoV-2 infection and potentially contribute to differences in COVID-19 disease severity across life span.

In addition to its role in SARS-CoV-2 infection, ACE2 regulates vascular homeostasis as part of the renin-angiotensin system (*7*). In this normal physiological role, ACE2 is expressed on cell membranes in a number of tissues outside the lung. Several single-cell transcriptomic analyses have been performed to determine the tissue and cell type distribution of *ACE2* expression (*8*–*11*). Although they have identified cell types that may be susceptible to infection, these studies generally lack data across different ages and are unable to examine ACE2 translation and localization. Protein-level measurements, therefore, are required to determine whether *ACE2* mRNA expression correlates robustly with translated, membrane-localized protein expression.

Viral entry represents just one of several steps in COVID-19 pathogenesis, each of which involves genes that may potentially be developmentally regulated in the lung and elsewhere. Apoptotic and nonapoptotic host cell death pathways also play important roles, as they can modulate disease pathogenesis after viral infection (*12*, *13*). Specifically, coronavirus-infected cells typically experience endoplasmic reticulum (ER) stress due to the intensive production of infectious virions and activate the unfolded protein response (UPR) to adapt to this stress (*14*). If the ER stress is overwhelming, then the cell undergoes intrinsic apoptosis (programmed cell death) by upregulating proapoptotic proteins—this serves as a host defense mechanism by arresting virion production. Virally encoded proteins may suppress this process during infection to enhance virion production (*15*–*17*). Intrinsic apoptosis is controlled by the members of the B-cell lymphoma-2 (BCL-2) family of proteins, which have prodeath or prosurvival roles in modulating mitochondrial release of cytochrome c, the commitment point for intrinsic apoptosis (*18*). We have previously found that apoptosis is dynamically regulated

[1]Molecular and Integrative Physiological Sciences Program, Harvard T.H. Chan School of Public Health, Boston, MA, USA. [2]Harvard Program in Therapeutic Science, Harvard Medical School, Boston, MA, USA. [3]Department of Pediatrics, University of California San Diego, La Jolla, CA, USA. [4]Image and Data Analysis Core, Harvard Medical School, Boston, MA, USA. [5]Integrated Cellular Imaging Core, Emory University, Atlanta, GA, USA. [6]Department of Medicine, University of California San Diego, La Jolla, CA, USA. [7]Sanford Burnham Prebys Medical Discovery Institute, La Jolla, CA, USA. [8]Sanford Consortium for Regenerative Medicine, La Jolla, CA, USA. [9]Department of Surgery, University of California San Diego, La Jolla, CA, USA. [10]Department of Medicine, Massachusetts General Hospital, Boston, MA, USA. [11]Department of Surgery, Johns Hopkins University, Baltimore, MD, USA. [12]Harvard Medical School, Boston, MA, USA.
*Corresponding author. Email: sarosiek@hsph.harvard.edu
†These authors contributed equally to this work.

during life span in multiple organs as they grow and mature (*19*); this dynamic regulation could affect the degree to which cells tolerate ER stress and thus the extent of virion production upon infection.

Here, we investigate how expression of viral entry and cell death genes in the lung might vary among different age groups and how this variation relates to known differences in disease severity. Using human lung specimens from more than100 donors along with transcriptional profiling and live virus experiments, we define novel correlates of COVID-19 disease severity and demonstrate that apoptosis, whether modulated physiologically or pharmacologically, can modulate cellular responses to SARS-CoV-2 infection and potentially curtail viral production.

RESULTS

ACE2 transcriptional regulation with age

In mouse and human lung, developmental processes in postnatal life require coordinated regulation of gene expression in epithelial and endothelial cells to ensure proper formation and maturation of airways and highly vascularized alveoli (*6*). The importance of ACE2 in maintaining vascular homeostasis suggests that it may also be dynamically regulated in the lung throughout life; variation in ACE2 expression may, in turn, affect cellular entry and infection by SARS-CoV-2 (*5*) and contribute to age-dependent differences in COVID-19 disease severity. On the basis of data from New York City Health and the U.S. Centers for Disease Control, although case rates do not differ markedly across ages, hospitalization and mortality rates have major age-based differences (Fig. 1, A to C). In particular, while children typically have lower severity, neonates and infants have a higher mortality rate than older children (Fig. 1C). On the other end of the age spectrum, individuals above the age of 65 have markedly higher hospitalization and mortality rates, which continue to increase further with age (Fig. 1, A to C). Although previous reports have investigated expression of *ACE2* in various adult cell types within the lung as well as in small intestine, kidney, and testis tissue (*8*–*11*), we sought to characterize how ACE2 expression changes at the transcript and protein levels across the mammalian life span to potentially affect disease severity.

To characterize ACE2 regulation during postnatal life, we first examined published gene expression data from mouse lung tissue at various developmental time points. Although some temporal and spatial aspects of lung maturation vary between mouse and human, the stages of lung development are similar across all mammalian species (*20*). In both the human and murine lung, alveologenesis (formation of highly vascularized alveoli, which are the primary gas exchange units in the lung) begins prenatally but is not complete until young adulthood (*20*) [~P36 (postnatal day 36) in mice and ~21 years of age in human (*21*, *22*)]. Furthermore, mouse models have become critical for research into coronavirus infection pathogenesis. In particular, these models have shown that host age, virus-host protein-protein interactions, and expression levels of viral receptors can all affect the "effective dose" of viral particles experienced by cells in the lung; this dosage can, in turn, determine the severity of symptoms (table S1) (*23*), although different engineered and naturally occurring SARS-CoV-2 variants may show varying infectivity in mice (*24*, *25*). Therefore, we queried expression of both *Ace2* and *Tmprss2* across 156 samples comprising 31 microarray experiments using a tool for combined analysis of published microarray data (*26*). We found that lung tissue collected from newborn mice (P0 to P3) exhibited higher *Ace2* expression levels than P4 to P15 adolescent mice and that expression increased steadily after adolescence through advanced age (P256+) (Fig. 1D). A similar expression pattern was observed for *Tmprss2*, although the magnitude of differences was smaller (fig. S1A). We confirmed these results in a separate set of 66 samples from five additional experiments using a distinct microarray platform (fig. S1, B and C).

For individual experiments from this collected dataset that included detailed time course data, patterns matched those observed in the combined data. Analysis of gene expression in P0, P3, P10, and P42 mice showed only minor changes in *Tmprss2* levels in whole lung and trachea, but *Ace2* expression was lower at P10 than all other time points in both tissues (*27*) (Fig. 1E). *Ace2* and *Tmprss2* were expressed at high levels in alveolar macrophages at P0 before declining substantially at P3 and later (fig. S1D). Similarly, *Tmprss2* and *Ace2* levels were highest immediately after birth in a study of lung tissue at P0, P1, and P3 (Fig. 1F) (*28*). Another study of tissue from P1, P8, and P28 mice did not show a decline in *Ace2* levels at P8 but did show elevated expression at P28 (fig. S1E) (*29*). Thus, across a diverse set of microarray datasets, lung *Ace2* levels were relatively high immediately after birth, significantly lower during adolescence, and increased in adulthood, reaching their peak at advanced age.

To complement these microarray data, we queried the Lung Gene Expression Analysis (LGEA) database of mouse RNA sequencing (RNA-seq) data across developmental time points (*30*). We again found that expression of *Ace2* and *Tmprss2* peaked around birth, declined in young mice, and increased again in older mice (Fig. 1G and fig. S1F). In sorted cells from the LGEA dataset, *Ace2* levels in epithelial cells were high at birth and were reduced shortly after, followed by an up-regulation when alveologenesis is nearing completion (Fig. 1H) (*20*). *Ace2* expression in vascular endothelial cells peaked at birth and then decreased by P30. *Tmprss2* was similarly expressed during this time period (fig. S1G).

To compare these mouse transcriptional data with human expression, we analyzed the LungMAP database, which contains RNA-seq data for sorted human lung cell types from donors of varying age (*31*). Consistent with murine data, human epithelial cell expression of *ACE2* and *TMPRSS2* was detected in neonates, infants, children, and young adults (24 to 40 years of age), with the highest levels evident in infant lung tissue (Fig. 1, I and J). Endothelial cells within the human lung expressed higher *ACE2* in adults than at other ages, although the sample size was limited.

These mouse and human data showed similar trends in expression by bulk RNA-seq, but the sorting strategy used in this analysis combined epithelial cells of various subtypes. Previous reports have demonstrated expression of *Ace2* specifically in alveolar type 2 (AT2) epithelial cells (*8*, *10*); we sought to determine whether this expression might vary with time. In single-cell RNA-seq data for AT2 cells and their embryonic precursors, we found that *Ace2* and *Tmprss2* can be expressed in AT2 cells as early as embryonic day 12 through P7 (Fig. 1K and fig. S1H). In middle adulthood (4 months), single-cell RNA-seq data showed that AT2 cells may express *Ace2* and *Tmprss2*, but broader expression was detected in bronchiolar epithelial cells including club and goblet cells (Fig. 1, L to P). Together, these data strongly suggested that *Ace2* is dynamically expressed in major lung cell types during postnatal life, potentially modulating (in concert with *Tmprss2* and other proteases) the number and type of cells susceptible to SARS-CoV-2 infection (summarized in table S2).

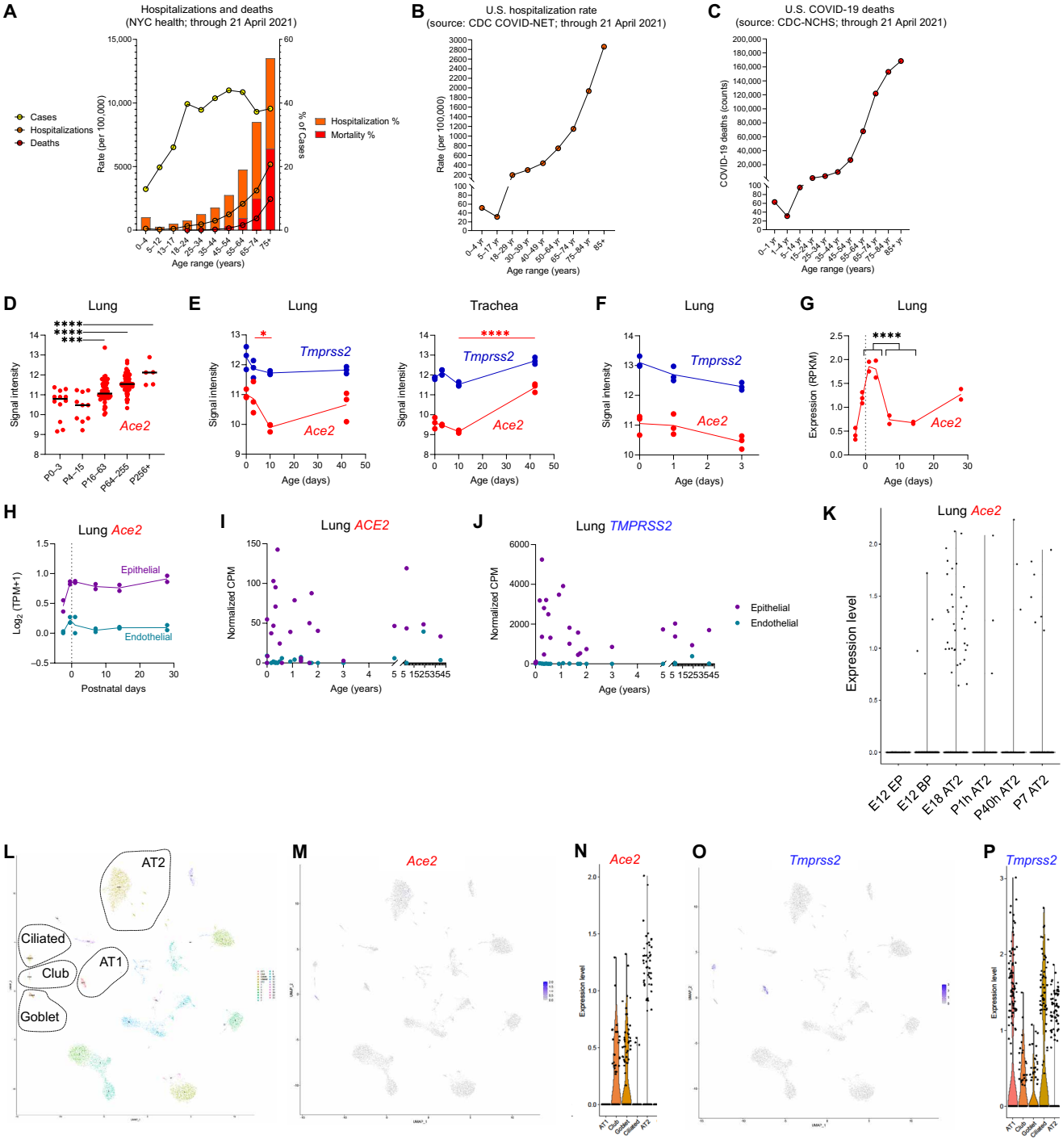

Fig. 1. ACE2 and TMPRSS2 are dynamically regulated postnatally in the mouse and human lung. (**A**) COVID-19 case statistics for New York City (NYC) as of 21 April 2021. Case (SARS-CoV-2+ tests), hospitalization, and death rates are presented per 100,000 population (left axis) or as percentage of cases (right axis). (**B** and **C**) COVID-19 hospitalization (B) and mortality (C) rate per 100,000 population in the United States as of 21 April 2021. CDC-NCHS, Center for Disease Control National Center for Health Statistics. (**D** to **F**) Mouse microarray gene expression data. (D) Collected data from experiments conducted on mouse lung tissue of the indicated age ranges using the Affymetrix Mouse Genome 430 2.0 array. Comparison between groups was conducted by one-way analysis of variance (ANOVA) with Holm-Sidak's adjustment. *$P < 0.05$, ***$P < 0.001$, and ****$P < 0.0001$. (E) Expression of *Ace2* and *Tmprss2* in mouse lung and trachea. (F) Expression of *Ace2* and *Tmprss2* in whole lung. (**G**) RNA sequencing (RNA-seq) data showing *Ace2* expression in whole lung. RPKM, reads per kilobase of transcript, per million mapped. reads. (**H**) RNA-seq data showing *Ace2* expression in FACS-sorted cell types from mouse lung. TPM, transcripts per kilobase million. (**I** and **J**) RNA-seq data showing *ACE2* (I) and *TMPRSS2* (J) expression in FACS-sorted cell types from human lung. (**K**) Single-cell RNA-seq showing *Ace2* expression in AT2 cells and their precursors (EP, epithelial progenitor; BP, bipotent progenitor) in mouse lung at the indicated pre- and postnatal time points. (**L**, **M**, and **O**) UMAP (uniform manifold approximation and projection) plots of adult mouse lung single-cell RNA-seq, showing cell type clusters (L) as well as expression of Ace2 (M) and *Tmprss2* (O). (**N** and **P**) Dot plots for selected cell types are shown alongside corresponding UMAP plots.

ACE2 expression in mouse lung tissue

We next sought to investigate these expression dynamics at the protein level directly in mouse lung tissue across life span. We stained for ACE2 and relevant cell markers in lung tissue from newborn (P0), young (P7), adult (3 months), and late adult (11 months) mice (Fig. 2). We detected slightly elevated levels of ACE2 across all nucleated cells immediately after birth, which were lower at P7 and increased by adulthood (3 months) (Fig. 2, A and B). We found that the higher perinatal ACE2 levels were at least in part attributable to its expression in aquaporin 3 (AQP3)–positive AT2 cells (Fig. 2, A and C), which was consistent with our gene expression analysis. Unexpectedly, we also found that ACE2 protein expression was strongly increased

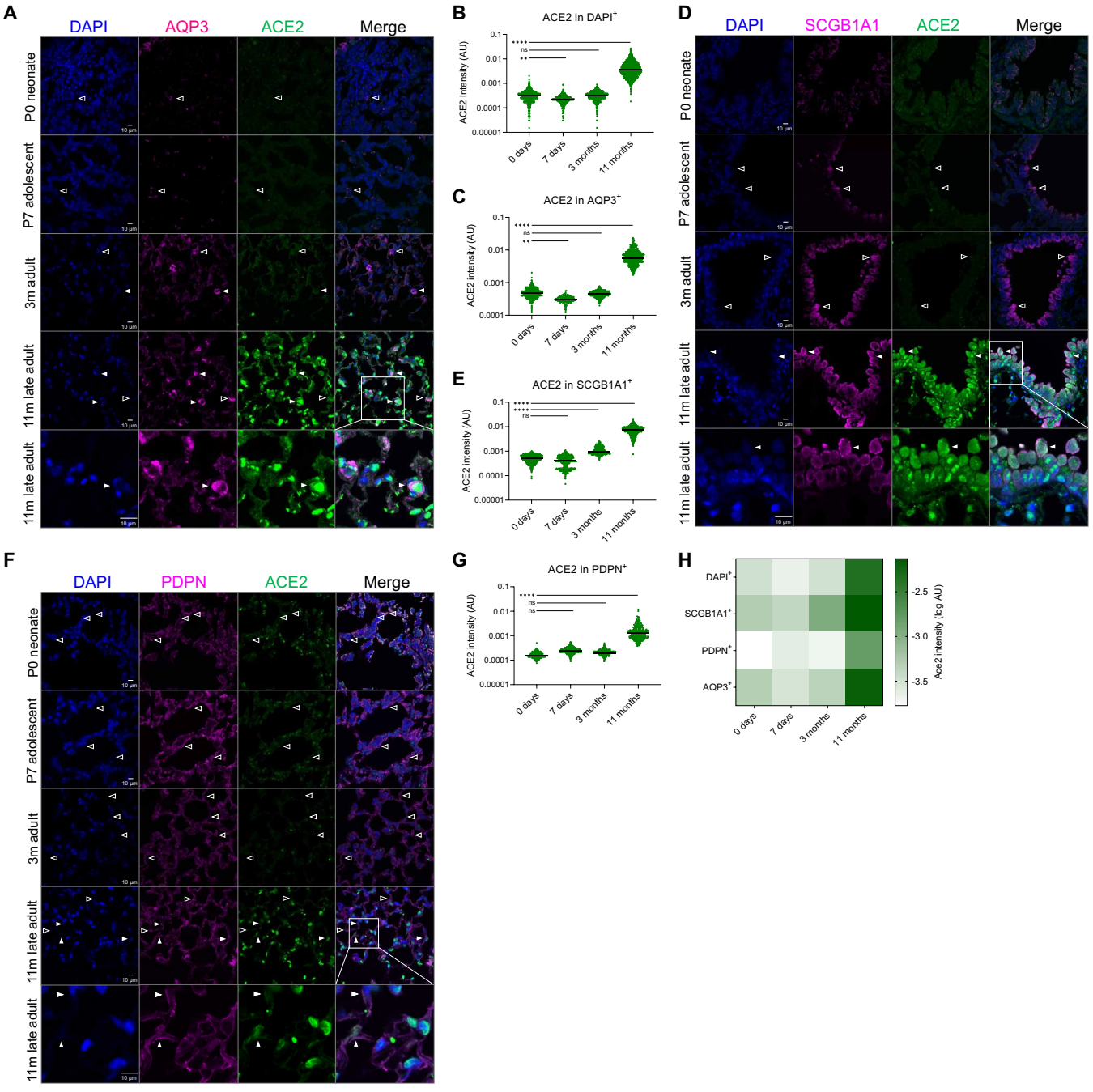

Fig. 2. Dynamic ACE2 expression in mouse postnatal lung. (**A**, **D**, and **F**) Images of immunofluorescence staining for ACE2 and other indicated proteins in lung tissue from mice at the indicated ages. Filled arrowheads indicate examples of cells that are positive for indicated marker and also positive for ACE2, while empty arrowheads are positive solely for the indicated marker but not ACE2. Scale bars, 10 μm. SCGB1A1, secretoglobin 1A1. (**B**, **C**, **E**, and **G**) Quantification of ACE2 fluorescence in all cells (B) or in cells with indicated marker (C, E, and G). Comparison between groups was conducted by one-way ANOVA with Holm-Sidak's adjustment. ns, not significant; AU, arbitrary units. $^{**}P < 0.01$ and $^{****}P < 0.0001$. (**H**) Comparison of average ACE2 staining intensities across cell types tested. m, months.

by late adulthood in AT2 cells and that it was expressed throughout the cell including the nucleus (Fig. 2A). We also stained for secretoglobin 1A1, a marker for club cells within the airway (Fig. 2, D and E), and found that expression levels were high at P0, slightly downregulated by P7, and increased at later ages. Last, faintly $ACE2^+$ cells were observed that could be AT1 given their proximity to podoplanin (PDPN) (Fig. 2, F and G), but further experimental confirmation would be required to confirm AT1 identity (see Discussion).

ACE2 expression in human lung tissue

The shifting expression of ACE2 in the mouse lung suggested that regulation in human lung tissue may also be dynamic. To test this, we stained for ACE2 and cell markers of interest in two tissue microarrays (TMAs) comprising more than 100 normal lung specimens from individuals ranging from 9 to 75 years of age. Because of the pronounced autofluorescence of red blood cells (Fig. 3A), we identified and segmented cells that stained positive for 4′,6-diamidino-2-phenylindole (DAPI) to evaluate total cellular ACE2 expression levels in 1,408,152 nucleated cells (Fig. 3B). We first determined the percentage of ACE2-positive cells among all nucleated ($DAPI^+$) lung cells across all individuals and found that lung tissue from older individuals had increased ACE2 positivity (Fig. 3, C and D). Furthermore, by linear regression analysis without (Fig. 3E) and with (Fig. 3F) the inclusion of donor tissue type (i.e., tissue from normal lung versus normal tissue adjacent to tumor) as a covariate, we obtained *P* values of 0.3073 and 0.03152, respectively, indicating that percentage of ACE2-expressing cells in the lung significantly increased with age when adjusting for tissue type. However, interindividual ACE2 positivity was highly heterogeneous across all ages (Fig. 3G): While some normal lung tissues from similarly aged individuals contained a high percentage of $ACE2^+$ cells (>70% of $DAPI^+$), others expressed almost no $ACE2^+$ cells (~0% of $DAPI^+$) (Fig. 3, C and D). We also performed a permutation test to examine whether intraindividual heterogeneity (i.e., variation in ACE2 florescence intensity between cells in a given tissue core) increased with age and found no significant correlation (fig. S2A).

We next sought to identify the cell types in which ACE2 was expressed by costaining for PDPN, a marker commonly expressed on AT1 cells that are responsible for gas exchange. We detected increasing ACE2 expression in $PDPN^+$ cells with advancing age (*P* values of 0.0182 without and 0.02221 with the inclusion of donor tissue type as a covariate) (Fig. 3, H to K). However, extensive heterogeneity was again evident across all ages (Fig. 3, H to L, and fig. S2B). Although we observed $PDPN^+$ $ACE2^+$ cells, the morphology was cuboidal, suggesting that they are potentially AT2 cells. While PDPN is detected in these cells, it was observed primarily in intracellular puncta rather than on the luminal surface found commonly on AT1 cells. This limitation in staining and interpretation may be due to the tissue being sourced from patients at autopsy or from normal lung tissue adjacent to tumors; either of these may reduce the specificity of PDPN staining for AT1 cells as has been previously reported (*32*). Last, although lung specimens from male donors tended to have higher expression of ACE2 in nucleated (fig. S2C) and $PDPN^+$ (fig. S2D) cells than female donors, the differences were not statistically significant, and similar age-based trends were evident for both sexes.

We next assessed levels of ACE2 expression specifically in AT2 cells by staining for AQP3 in the two TMAs. In contrast with $PDPN^+$ cells, expression of ACE2 did not increase with age in AT2 cells in these specimens (Fig. 4, A to F), although several of the specimens were removed from analysis due to inadequate specimen quantity or quality (see Materials and Methods). The expression of ACE2 was again highly heterogeneous (Fig. 4, B, C, and F, and fig. S2E) with similarly aged individuals expressing a wide range of ACE2 positivity (from ~0 to >90%). Since our TMAs did not contain specimens from neonates or infants, we obtained neonatal lung tissue to assess the early-life expression of ACE2 in human lung tissue. We detected ACE2 expression on the apical surfaces of airway epithelial cells in infant (3 to 5 months of age) lung tissue (Fig. 4G) and in cells outside of the airways (Fig. 4H). Thus, we detected age-based differences in ACE2 expression in multiple cell types within the mouse and human lung (tables S2 and S3), which may delineate the pool of cells that can be infected by SARS-CoV-2 at different ages. Intriguingly, changes in ACE2 expression, which are heterogeneous but broadly consistent across mouse and human samples, are correlated with COVID-19 disease severity in human patients (Fig. 1, A to C).

Confirming apoptosis in SARS-CoV-2 infection

Our results, thus far, suggested that higher lung ACE2 expression in infancy and late adulthood would broaden the pool of cells that can be potentially infected by SARS-CoV-2 at those ages. At all ages, however, ACE2 expression was highly variable between individuals, indicating that humans of any age can potentially be infected by SARS-CoV-2 throughout the respiratory system. This variability also led us to conclude that ACE2 expression patterns were insufficient to explain the broader differences in disease severity. We therefore sought to characterize how apoptosis is regulated in respiratory tissues, since cells can trigger apoptosis as a host defense mechanism against viral infection to curtail virion production (*12*, *13*).

We first confirmed the relevance of studying this cell death pathway in SARS-CoV-2 infection by examining lung tissue from patients with terminal COVID-19 for evidence of apoptosis. We detected extensive cleaved (activated) caspase 3 in nucleated cells within COVID-19 postmortem lung tissue but not lung tissue from healthy control subjects (Fig. 5A). To rule out apoptosis occurring solely in immune cells, we costained with CD45 and demonstrated a lack of overlap with cleaved caspase 3 (Fig. 5B).

In the case of coronaviruses, active infection and stimulation of virion production typically results in proteotoxic ER stress and consequent activation of the UPR (*16*), which is also a potent inducer of apoptotic cell death (*33*, *34*). Notably, apoptosis can be suppressed during infection by virally encoded proteins to prolong virion production (*15*–*17*). We therefore investigated how the expression of BCL-2 family genes changed in response to SARS-CoV-2 infection in a recently reported study (*35*). We first confirmed that productive SARS-CoV-2 infection of lung cell lines Calu-3 and A549 [both wild type (WT) and ACE2 overexpressing] potently activates the UPR as evidenced by the up-regulation of canonical UPR-associated genes *ATF4* and *DDIT3* (CCAAT/enhancer binding protein homologous protein) (Fig. 5C). Furthermore, active infection also induced expression of potent proapoptotic activator protein BIM (BCL-2-interacting mediator of cell death; encoded by *BCL2L11*) and especially the endogenous MCL-1 (myeloid cell leukemia 1) inhibitor protein Noxa (*PMAIP1*) (Fig. 5C and fig. S3A). Up-regulation of Noxa is sufficient to induce apoptosis in MCL-1–dependent cells (*36*, *37*) and enhances overall apoptotic priming as well as dependence on other prosurvival proteins such as BCL-2 or $BCL\text{-}X_L$ (*38*, *39*).

Apoptotic regulation in the maturing respiratory system

Having confirmed the relevance of apoptotic signaling to SARS-CoV-2 infection, we hypothesized that differences in apoptotic regulation by BCL-2 family proteins among cells within the respiratory system from birth to adulthood could alter cell fates and ultimately disease severity. Members of the BCL-2 family of genes play pro-death and prosurvival roles in modulating apoptosis (*18*), which may affect not only viral production but also tissue damage and immune responses. We assessed how BCL-2 family genes were regulated during postnatal lung maturation to potentially modulate cell fate in response to SARS-CoV-2 infection. In LGEA RNA-seq data, proapoptotic genes *Bcl2l11* (encoding BIM) and *Bmf* were both highly expressed in young mouse lung tissue; both peaked at P1 and declined over the remaining time points until P28 (late juvenile, early

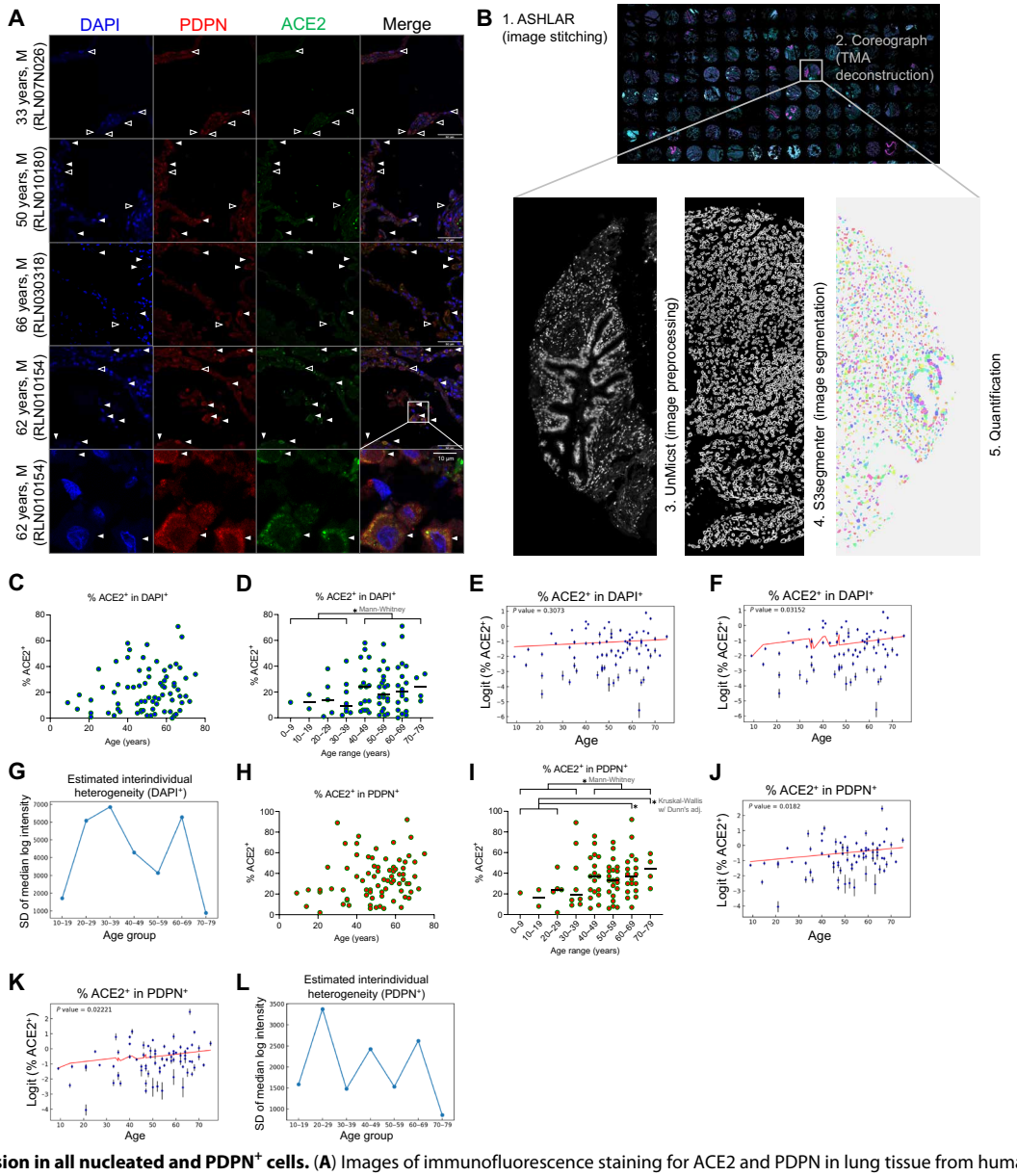

Fig. 3. ACE2 expression in all nucleated and PDPN$^+$ cells. (**A**) Images of immunofluorescence staining for ACE2 and PDPN in lung tissue from humans at the indicated ages. Filled arrowheads indicate examples of cells that are positive for indicated marker (PDPN) and also positive for ACE2, while empty arrowheads are positive solely for the indicated marker but not ACE2. Scale bars, 50 or 10 μm for magnified region of interest. (**B**) Schematic of image processing and quantification pipeline for human TMAs. Images are first acquired as single tiles on a wide-field fluorescence microscope and are stitched (ASHLAR). The TMA is separated into single organized cores (Coreograph), and the DAPI channel of each core is preprocessed to accentuate nuclei boundaries for easier segmentation (UnMicst). On the basis of this intermediate image, the nuclei and corresponding cytoplasmic regions are compartmentalized as separate indexed objects (S3segmenter), and the mean/median intensity of each is quantified. (**C**) Percent ACE2 positivity among all DAPI$^+$ cells from each donor, plotted against donor age. (**D**) Comparison of ACE percent positivity among age groups. *$P < 0.05$. (**E** and **F**) Correlation analysis comparing age with percent ACE2 positivity in all cells in lung tissue TMAs. Data points represent logit-transformed % positive values, and error bars represent ±2 σ_i, where σ_i is the estimated SD. Red lines show the linear regression fit of $Y_i \sim 1 + \text{age}_i$ (E) or $Y_i \sim 1 + \text{age}_i + \text{type}_i$ (F) where type_i represents the type of tissue (i.e., normal lung or NAT). The *P* values shown are for testing for nonzero coefficient for age. (**G**) Weighted SD of median ACE2 signal intensity in TMA cores from the age ranges shown. (**H** to **L**) Analysis as in (C) to (G) for the subset of PDPN $^+$ cells.

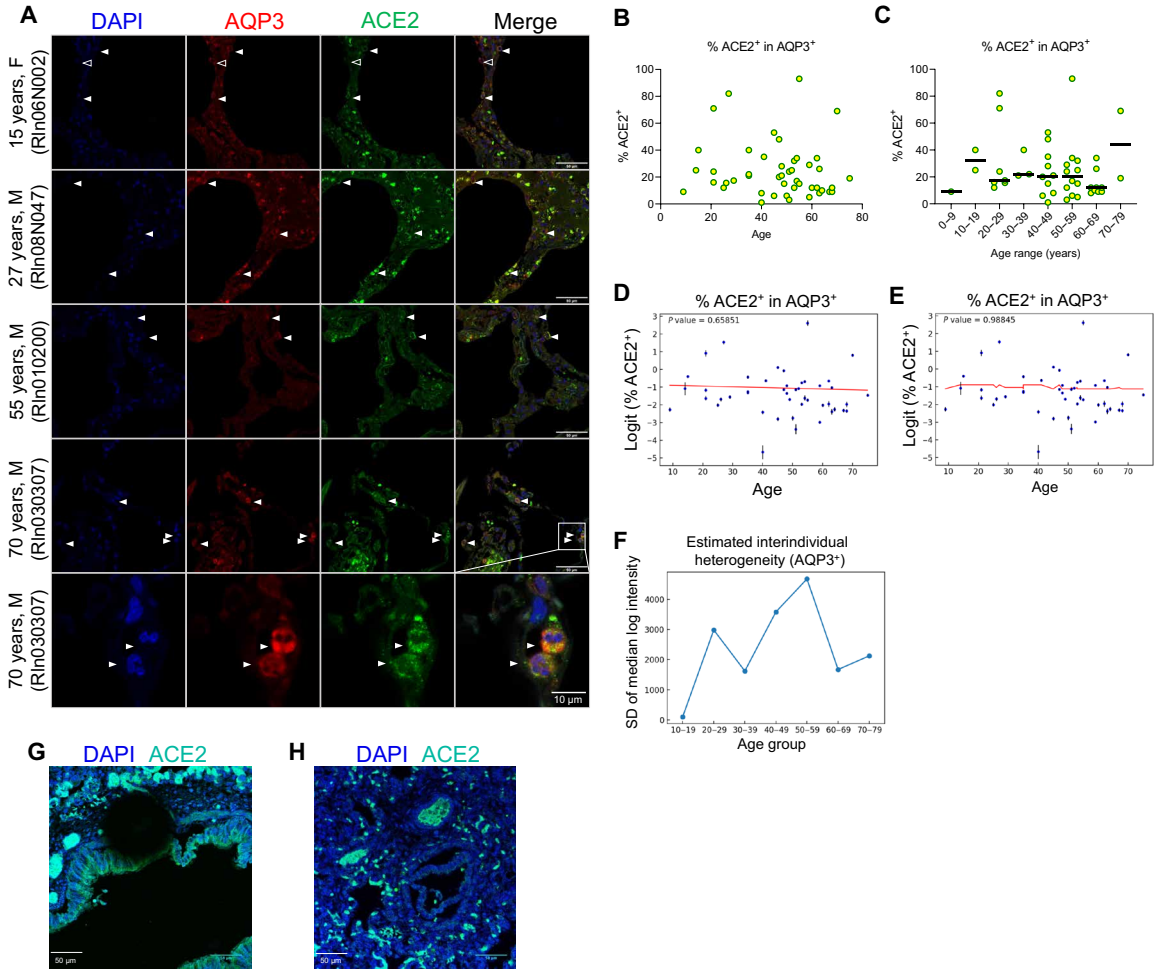

Fig. 4. ACE2 expression in human AT2 cells. (**A**) Images of immunofluorescence staining for ACE2 and AQP3 in lung tissue from humans at the indicated ages. Filled arrowheads indicate examples of cells that are positive for indicated marker (AQP3) and also positive for ACE2, while empty arrowheads are positive solely for the indicated marker but not ACE2. Scale bars, 50 or 10 μm for magnified region of interest. (**B**) Percent ACE2 positivity among all DAPI$^+$ cells from each donor, plotted against donor age. (**C**) Comparison of ACE percent positivity among age groups. (**D** and **E**) Correlation analysis comparing age with percent ACE2 positivity in all cells in lung tissue TMAs. Data points represent logit-transformed % positive values, and error bars represent ±2 sigma_*i*, where sigma_*i* is the estimated SD. Red lines show the linear regression fit of *Y_i* ~ 1 + age_*i* (D) or *Y_i* ~ 1 + age_*i* + type_*i* (E) where type_*i* represents the type of tissue (i.e., normal lung or NAT). The *P* values shown are for testing for nonzero coefficient for age. (**F**) Weighted SD of median ACE2 signal intensity in TMA cores from the age ranges shown. (**G** and **H**) Images of immunofluorescence staining for ACE2 in neonatal human lung tissue (3 to 5 months of age). Scale bars, 50 μm.

adult) (Fig. 5D and fig. S3, B and D). Among prosurvival BCL-2 family members, *Mcl1* was most highly expressed and similarly peaked at P1, as did the more moderately expressed *Bcl2* (fig. S3E). In contrast, expression of *Bcl2l1* (coding for prosurvival BCL-X_L protein) was low in P1 mice but increased by P28. *Bax* and *Bak1*, which encode pore-forming proteins that trigger the apoptotic cascade when proapoptotic Bcl-2 family members overwhelm prosurvival family members, were expressed at levels likely sufficient to allow apoptosis execution at all time points (fig. S3F).

We next tested whether similar expression changes in BCL-2 family genes would be evident in human lung tissue. We examined BCL-2 family RNA-seq data in epithelial cells within the LungMAP database and found that expression patterns were largely consistent with mouse data while also demonstrating higher heterogeneity. Proapoptotic *BCL2L11* and *BMF* were again expressed at increased levels in early life (neonates) and reduced in adult lung tissue, while prosurvival *MCL1*, *BCL2A1* (encoding BFL-1/A1), and *BCL2L1* (BCL-X_L) increased with age (Fig. 5, E to G, and fig. S3, C and G to I). These changes, consistent with a decrease in apoptotic priming over time, were observed predominantly in epithelial and endothelial cells of the human lung.

These gene expression patterns suggested that young lung tissue would be more prone to undergoing apoptotic cell death. We evaluated this at the functional level using BH3 profiling, an assay that measures apoptotic priming and dependencies by testing mitochondrial sensitivity to titrated doses of apoptosis-inducing peptides (Fig. 5H and fig. S3J) (*40*). We found that lung epithelial cells [positive for epithelial cell adhesion molecule (EPCAM)] are highly primed for apoptosis (more prone to activating apoptosis in response to damage or stress) at early age as evidenced by higher levels of

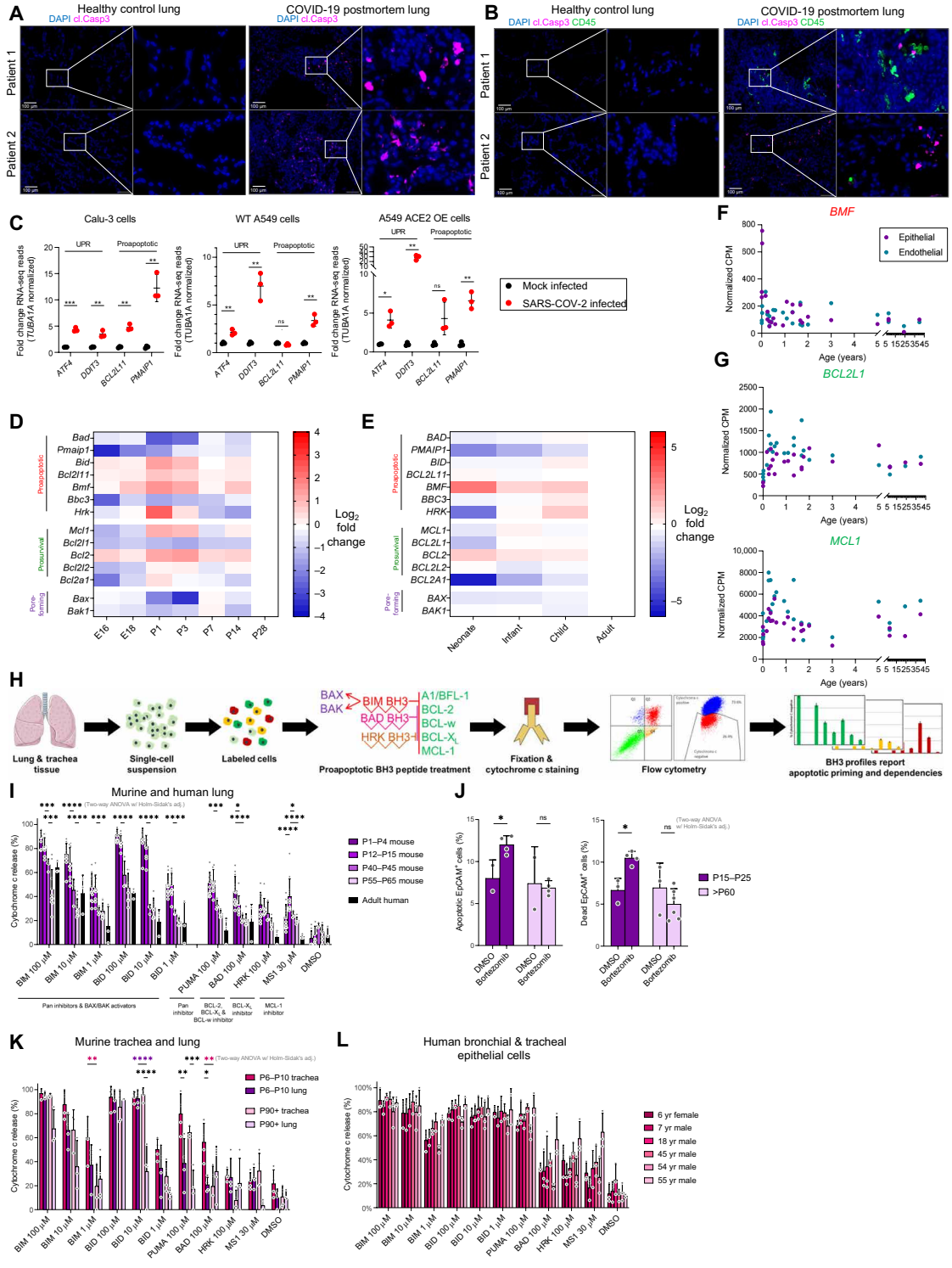

Fig. 5. Changing expression of cell death-associated genes may modulate outcomes in children versus adults. (**A** and **B**) Immunofluorescence imaging of postmortem human lung tissue from patients with COVID-19 and healthy control donors. Scale bars, 100 μm. (**C**) RNA-seq data for selected UPR and cell death genes in mock and SARS-CoV-2–infected cell lines. (**D** and **E**) Absolute expression levels of Bcl-2 family genes as measured by RNA-seq of sorted lung epithelial cells in mouse (D) and human (E). (**F** and **G**) RNA-seq data showing proapoptotic *BMF* (F) and prosurvival *BCL2L1* and *MCL1* (G) expression in FACS-sorted cell types from human lung. (**H**) Schematic showing protocol for BH3 profiling assay. (**I**, **K**, and **L**) Apoptotic priming of mouse and human lung tissue (I), mouse lung and tracheal tissue (K), and human primary bronchial/tracheal epithelial cells (L) as measured by BH3 profiling. Data represent percentage cytochrome c release upon application of activator or sensitizer BH3 peptides. Comparison between groups was conducted by two-way ANOVA. $^{*}P < 0.05$, $^{***}P < 0.001$, and $^{****}P < 0.0001$. (**J**) Caspase activation and cell death in EpCAM^{+} lung epithelial cells collected from mice treated with bortezomib (2.5 mg/kg) or vehicle control.

cytochrome c release in response to proapoptotic BIM or BID (BH3-interacting domain death agonist) BH3 peptides in young (P1 to P15) versus older lung tissue (Fig. 5I). Adult lung epithelial cells were more resistant to apoptosis, but the pathway remained intact as indicated by continued sensitivity to higher concentrations of activator BH3 peptides BIM and BID. The intact yet suppressed state of the apoptosis pathway was also evident in lung epithelial cells from adult human subjects (Fig. 5I). BH3 profiling also demonstrated that lung epithelial cells in the youngest mice were dependent on BCL-2 and/or BCL-X_L for survival but that this dependence switched to MCL-1 in the P12 to P15 animals (Fig. 5I). To test whether these differences in apoptotic priming may affect the induction of apoptosis by SARS-CoV-2–induced ER stress and UPR, we treated mice at young or adult ages with the proteosome inhibitor bortezomib, a well-established activator of ER stress (*41*). Consistent with our priming results, we detected increased caspase-active and dead epithelial cells in young but not adult mice treated with this agent (Fig. 5J).

Since airway epithelial cells also express *ACE2* and are a potential target for SARS-CoV-2 infection (*11*), we also BH3-profiled mouse tracheal epithelial cells to determine if their regulation of apoptosis was similar to epithelial cells in the distal lung. Although we detected an age-based down-regulation of apoptotic priming in these tracheal epithelial cells (Fig. 5K), these cells were considerably more primed at adulthood than those in the lung, indicating that age-based suppression of apoptosis is most strongly evident in the distal lung. The differences in apoptotic priming between lung and trachea were consistent with gene expression from the Tabula Muris database of single-cell RNA-seq from various mouse tissues (fig. S3K). In these data, tracheal tissue from male and female mice expressed lower levels of the antiapoptotic genes *Bcl2l2* and *Bcl2a1*, as well as higher levels of the proapoptotic gene *Pmaip1* (NOXA) and the antiapoptotic gene *Bcl2*.

To test the apoptotic priming of tracheal cells from human tissue, we cultured primary human tracheal and bronchial epithelial (HTBE) cells from six donors aged 6 to 55 years in an air-liquid interface (ALI) to induce epithelial differentiation. We BH3-profiled these well-differentiated cells and found that all six were highly primed for apoptosis and there was no significant difference in priming levels between donors (Fig. 5L). Although our sample size was limited, the lack of apoptotic priming differences between primary cells from young and old human donors suggests that environmental, physiological, pathophysiological, and other factors likely affect apoptotic regulation in airway epithelial cells. Further, their consistently high level of priming suggests that bronchial and tracheal epithelial cells would have more similar cell fates than alveolar epithelial cells when infected with SARS-CoV-2 regardless of age.

Overall, these data demonstrate that infection of distal lung epithelial cells would trigger apoptosis more quickly and readily in the young lung than in the adult, potentially curtailing virion production in young individuals. Heightened apoptotic sensitivity in virus-infected cells has been previously shown to decrease virion production, infection severity, and host mortality (*12*, *14*, *16*, *42*, *43*); we therefore proceeded to investigate whether this would hold true directly in SARS-CoV-2–infected cells.

Modulation of apoptosis in SARS-CoV-2 infection

Since we had observed that SARS-CoV-2 infection induces UPR and transcriptional changes that increase apoptotic signaling and potentially drive increased dependence on BCL-2 or BCL-X_L, we reasoned that infected cells could be selectively eliminated using inhibitors of these proteins. To test this hypothesis, we first tested whether apoptosis induced by bortezomib treatment and subsequent UPR could be modulated using BH3 mimetics. BH3 mimetics are novel drugs that inhibit the prosurvival activity of specific BCL-2 family proteins (*18*); used either alone or in combination, they can exploit the apoptotic priming and dependencies of a given cell population by triggering apoptosis. Highly potent and specific BH3 mimetics have been recently developed and Food and Drug Administration (FDA)–approved for use as therapeutics for certain cancers including leukemias and lymphomas (*44*, *45*). We tested BH3 mimetics in two models of human respiratory cells: BEAS-2B lung epithelial cells (fig. S4A) and the human primary bronchial and tracheal epithelial cells in which we had performed BH3 profiling (fig. S4B). In both systems, bortezomib treatment alone resulted in minimal cell death as measured by annexin V and propidium iodide (PI) staining, but apoptosis was greatly enhanced by the addition of BH3 mimetics. No major differences in bortezomib or BH3 mimetic sensitivity was observed between primary cell donors, consistent with the earlier BH3 profiling data.

To test whether these findings would hold in the context of live viral infection, we modulated apoptosis in SARS-CoV-2–infected Vero African green monkey kidney epithelial cells using BH3 mimetics (Fig. 6, A and B). When we monitored cell death in Vero cells following SARS-CoV-2 infection, we found that treatment with ABT-199 (an inhibitor of BCL-2) or ABT-737 (an inhibitor of BCL-2, BCL-X_L, and BCL-w) substantially enhanced virus-induced cell death relative to vehicle control (Fig. 6, C and D). The MCL-1 inhibitor S63845 did not significantly increase virus-induced apoptosis (Fig. 6, C and D), consistent with the transcriptional up-regulation of the endogenous MCL-1 inhibitor *PMAIP1* (encoding Noxa) and expected consequent dependence on BCL-2 and BCL-X_L in infected cells. However, combining the MCL-1 inhibitor with ABT-199 or ABT-737 further accelerated apoptosis in infected cells (Fig. 6, C and D).

We confirmed that SARS-CoV-2–induced cell death was apoptotic by detecting activation of caspases and externalization of phosphatidylserine (annexin V binding) (Fig. 6E), both hallmarks of apoptotic cell death. Both of these signals were strongly enhanced by treatment with the BH3 mimetics ABT-737 and the specific BCL-XL inhibitor A-1331852 and entirely prevented by the pan-caspase inhibitor Q-VD-OPH [quinolyl-valyl-O-methylaspartyl-(2,6-difluorophenoxy)-methyl ketone] (Fig. 6, E to H). Collectively, these results indicate that cells infected with SARS-CoV-2 experience apoptotic stress and are rapidly and selectively eliminated by treatment with BH3 mimetics, especially those targeting BCL-X_L.

Expression of ACE2 in extrapulmonary tissues

While impairment of lung function is a major source of morbidity and mortality for patients with COVID-19, severe damage to the cardiovascular, renal, and gastrointestinal (GI) systems by SARS-CoV-2 is also evident in patients with poor outcomes (*46*). We therefore compared the expression of SARS-CoV-2 cell entry genes across major organs and found that *ACE2* expression in human lung was low, and *TMPRSS2* expression was high, relative to other organs (fig. S5A)—this is consistent with our immunofluorescence analysis showing cell type–specific lung expression of ACE2 at most ages. Throughout the respiratory system, *TMPRSS2* and *ACE2* were broadly expressed and, consistent with previous reports, *ACE2* expression was particularly high in the nasopharynx (*11*, *47*). Also

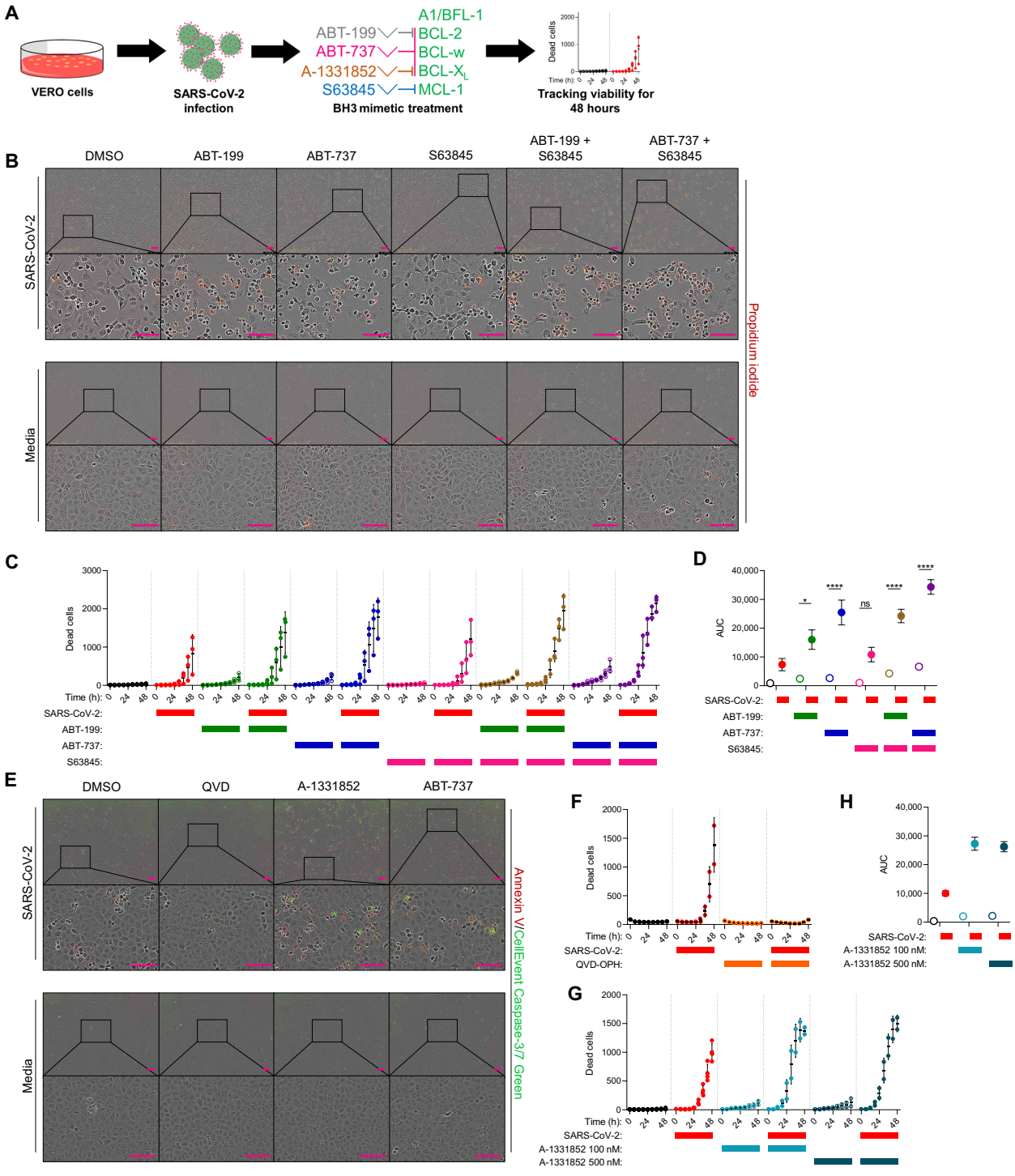

Fig. 6. BH3 mimetics promote apoptosis of virus-infected lung cells. (**A**) Schematic showing protocol for live virus experiments using BH3 mimetics. (**B**) Measurements of cell death (PI staining) of Vero cells infected with SARS-CoV-2 virus [multiplicity of infection (MOI), 1] in the presence or absence of indicated BH3 mimetics (625 nM) at 36 hours post infection. Scale bars, 100 μm. (**C**) Cell death (PI staining) tracking over 48 hours of BH3 mimetic treatment of Vero cells infected with SARS-CoV-2 (MOI, 1). (**D**) Area under the curve (AUC) values calculated from (C). Values were compared by two-way ANOVA with Dunnett's multiple comparison test for significance. $*P < 0.05$ and $****P < 0.0001$. (**E**) Images of SARS-CoV-2–infected and SARS-CoV-2–uninfected Vero cells treated with the caspase inhibitor Q-VD-OPh (10 μM), the BCL-X_L inhibitor A-1331852 (100 nM), or the Bcl-2/BCL-X_L inhibitor ABT-737 at the specified concentrations. Cell death was measured by caspase cleavage (CellEvent Caspase-3/7 Green) and phosphatidylserine (PS) externalization (annexin V). (**F**) Tracking of Vero cell death over 48 hours in the presence or absence of SARS-CoV-2 (MOI, 1) and/or 10 μM Q-VD-OPh. (**G**) Tracking of cell death over 48 hours in the presence or absence of SARS-CoV-2 infection and/or the BCL-X_L inhibitor A-1331852 at the indicated doses. (**H**) AUC calculated from (G).

consistent with previous reports (*48*), *ACE2* expression was high in several extrapulmonary tissues, including human testis, kidney, and GI tract—several of these were confirmed at the protein level by mass spectrometry (fig. S5, A and B) (*49*).

Last, we extended our age-dependent gene expression analysis to additional human tissues to examine how *ACE2* and *TMPRSS2* levels might change over life span. While cardiac tissue expressed *ACE2* throughout prenatal and postnatal life, expression levels were particularly high in early childhood and then declined with age (fig. S5C) (*50*). It is unclear whether this may be linked to the increasing evidence of cardiac dysfunction in young children diagnosed with COVID-19 (whether via the enzymatic function of ACE2 or its role as a viral entry receptor) (*51*, *52*). A similar pattern was observed in testis tissue (fig. S6D). Little or no *ACE2* expression was detected across life span in the brain or liver (fig. S6, E and F); limited postnatal expression data were available for kidney and ovary tissue, but available time points showed moderate expression in the former and low expression in the latter (fig. S6, G and H). Proteomic and genomic measurements were mismatched for some tissues (e.g., ovary), suggesting potential posttranscriptional regulation of ACE2 levels (fig. S6I).

DISCUSSION

Our studies provide evidence that ACE2, TMPRSS2, and apoptotic programs are dynamically regulated by age and cell type in the lung and correlate with severity of COVID-19 disease. On the basis of our study and our current understanding of SARS-CoV-2 infection, we propose that increased expression of ACE2 in airway and alveolar epithelial cells in infancy and old age contributes to the increased severity of COVID-19 symptoms in these populations (tables S2 and S3). Furthermore, the strong up-regulation of ACE2 in late adulthood across multiple cell types in the lung increases the number of cells that can potentially be infected by SARS-CoV-2. ACE2 expression on fragile AT1 cells could be especially problematic given their roles in barrier function and gas exchange. In severe cases of COVID-19, leakage of blood plasma and interstitial fluid into the airspace can occur, along with severe inflammation and hyperproliferation of AT2 cells (*46*, *53*); rapid loss of infected AT1 cells would be expected to promote all these responses. Although we observed ACE2 expression in human lung cells expressing the AT1 marker PDPN, an AT2 costain and another AT1 marker (e.g., receptor for advanced glycation end products) would be required to confirm whether they are bona fide AT1 cells.

Our study also demonstrates that the apoptotic priming of young lung tissue is higher than in adults; this has been previously associated with decreased virion production due to earlier induction of apoptosis (*15*, *16*). Our results suggest that this mechanism, along with reduced ACE2 expression, may predispose children to a milder COVID-19 disease course.

Our study has limited racial diversity among donors of the TMA lung tissue. Only Asian individuals were represented in these TMAs, preventing analysis of racial or ethnic differences in ACE2 expression. However, given the substantial impact of social determinants of health on variable COVID-19 mortality rates among racial groups in the United States (*54*), it is perhaps unlikely that ACE2 expression is a major contributor to these racial disparities.

Our findings also suggest a potential therapeutic approach focused on cell death responses to infection, wherein apoptotic priming in adult lung tissue would be modulated to match that in pediatric lung. This approach, which could involve administration of BH3 mimetics [small-molecule BCL-2 family inhibitors (*44*)] systemically or directly to lung tissue via inhalation, would be expected to reduce virus replication in adults as infected, stressed cells would undergo apoptosis earlier, halting further virion production. We found that treatment with the BH3 mimetics ABT-737 accelerated the commitment to apoptosis in SARS-CoV-2–infected cells. This agent has been previously evaluated in clinical trials for several cancers and targeting of virus-infected cells with ABT-737 treatment represents an intriguing therapeutic approach (*55*). The efficacy of this approach is not likely to be specific to particular SARS-CoV-2 variants, and BH3 mimetic treatment might also be effective in other viral infections that similarly modulate apoptotic priming in host cells. The FDA-approved BCL-2 inhibitor ABT-199 (venetoclax) is commonly used as treatment for hematologic malignancies including chronic lymphocytic leukemia and acute myeloid leukemia (*56*, *57*); this well-tolerated agent may therefore be best suited for initial clinical evaluation in early-stage SARS-CoV-2 infection. Notably, given the role of apoptotic cell death in suppressing inflammation, such a treatment might further reduce negative outcomes in infected patients by immune-mediated mechanisms (*58*). A recent report showed that patients with leukemia on venetoclax at time of COVID-19 diagnosis were hospitalized at rates similar to those on ibrutinib (*59*), which has been reported to exert a protective effect against SARS-CoV-2 induced pulmonary injury and is associated with improved outcomes (*59*, *60*). Also, the use of drugs that inhibit the activity of UPR proteins such as PERK or IRE1 may impair ER stress responses, increase apoptotic signaling, and accelerate the commitment to apoptosis in infected cells to reduce virion production (*16*, *61*). However, in each of these cases, the potential tissue damaging effects of apoptosis promotion require careful consideration.

Initial infection and cell death are only two of an extensive set of factors influencing disease course in patients with COVID-19 and other respiratory viruses. Immune response (*35*, *62*), host genetics (*63*), environmental factors (*8*), and therapeutic interventions (*64*, *65*) may all play contributing roles in determining infection outcome. Further, because of the dynamic regulation of blood pressure, fluid and electrolytes by the renin-angiotensin-aldosterone system (*66*), it is likely that inter- and intraindividual variation in ACE2 expression, perhaps even over short time scales in a single individual, will also affect disease course, consistent with the extreme heterogeneity in lung ACE2 expression we observed. Continued investigation will be required to determine how these mechanisms [e.g., (*11*)] control the expression of ACE2 expression over time. Nonetheless, our discovery of the age-dependent regulation of ACE2, TMRPRSS2, and apoptosis sensitivity in the lung sheds light on potential determinants of disease severity in COVID-19 and responses to lung insults more broadly.

MATERIALS AND METHODS

Animal care and use

Mouse tissue immunofluorescence experiments described in these studies were approved by the Johns Hopkins University Animal Care and Use Committee (protocol no. M019M332) and were performed according to the *Guide for the Care and Use of Laboratory Animals* of the National Institutes of Health. Male and female C57BL/6J mice were obtained from the Jackson laboratory (#000664, Bar Harbor, ME) and bred and housed in the Johns Hopkins animal facility.

For BH3 profiling and bortezomib treatment, cohorts of mice were housed and bred in a colony in accordance with the policies and regulations set forth by the Harvard TH Chan School of Public Health's Institutional Animal Care and Use Committee (IACUC), under protocol no. 5245. All animal experiments were approved by IACUC under HSPH protocol no. IS00001059-3. C57BL/6J (WT) mice (the Jackson laboratory) were used for tissue collection.

Human tissue samples

Human TMAs were obtained from US Biomax Inc. (Derwood, MD). Arrays LCN241 and LC2086a were selected to represent the broadest possible age range of donors, and overlapping donors from the two cores were excluded from analysis of LC2086a. Properties of the donors are shown in fig. S4. Morphology of the analyzed cores was examined by a pathologist for signs of lung disease; the pathologist's analysis is shown in fig. S4, and cores showing evidence of hemorrhage were excluded to avoid errors in quantification arising from the autofluorescence of red blood cells in the stained cores.

Human infant lung samples were obtained and processed at autopsy from either patients with necrotizing enterocolitis or age-matched infants that died from unrelated conditions that did not affect the lungs, with approval from the University of Pittsburgh Institutional Review Board (IRB; CORID no. 491) and in accordance with the University of Pittsburgh anatomical tissue procurement guidelines. All samples were deidentified via an independent honest broker assurance mechanism (approval no. HB#043) and transferred to Johns Hopkins University under the guidance of MTA (materials under agreement) approval (Johns Hopkins University MTA no. A26558) for analysis.

Lung tissue from human subjects who succumbed to COVID-19 at University of California San Diego (UCSD) was obtained via rapid post mortem tissue biopsy, with lung tissue harvested within 2 hours of death. Lung tissue was snap-frozen in liquid nitrogen and stored in a biosafety level 3 (BSL3) and −80°C freezer. All studies at UCSD were conducted on deceased human subjects, which were exempt from IRB oversight, as deceased patients are not considered human subjects' research by the U.S. FDA or U.S. Department of Health and Human Services.

Human lung tissue for BH3 profiling was obtained at the Massachusetts General Hospital Cancer Center in accordance with Dana Farber Cancer Institute IRB protocol no. 13-416. Tissue was obtained from three individuals: a 72-year-old female, a 60-year-old female, and a 78-year-old male. Donors underwent lobectomy for removal of cancerous tissue; pathological analysis was performed on the resected tissue, and the samples provided for the present study were considered normal.

Analysis of public gene expression databases

Mouse and human microarray data were analyzed using Genevestigator (NEBION, Zurich, Switzerland). Mouse data were filtered to exclude non-WT genetic backgrounds and experimental treatments. The remaining lung gene expression data were grouped by age and exported to generate plots. For human microarray data, samples were filtered to exclude disease conditions or drug treatments. The remaining data were grouped by anatomy. Some exported groups included broader (e.g., organ system) or narrower (e.g., organ and organ substructure) classifications; all the sample groups plotted were mutually exclusive.

RNA-seq data were obtained from the LGEA (*30*) and LungMAP (*31*) databases, with corresponding protein levels in extrapulmonary tissues confirmed using the Human Proteome Map (*49*) database. RNA-seq data from SARS-CoV-2–infected cell lines was obtained from Gene Expression Omnibus accession no. GSE147507 (*35*).

Single-cell RNA-seq

Previously published (*67*, *68*) single-cell RNA-seq datasets were analyzed for expression of genes of interest. Time course data were from accession no. GSE119228 and 4 month data were from accession no. GSE121611. Processing was performed using the Seurat package in R (*69*).

Tissue immunofluorescence sample preparation and imaging

Immunofluorescent staining of lung tissues was performed on 4% paraformaldehyde (PFA)–fixed 5-μm-thick paraffin sections. Mouse lung samples were perfused with 20 ml of normal saline through ventricle infusion immediately after humane euthanasia and inflated with 4% PFA through tracheal instillation and followed by fixation of the lung samples in 4% PFA (Electron Microscopy Sciences, #RT15700) in tris-buffered saline overnight and further processed in a Microm STP 120 Spin Tissue Processor (Thermo Fisher Scientific). Sections (5 μm) were cut from either paraffin blocks using a CUT 6062 microtome (SLEE Medical GmbH, D-55129, Mainz, Germany). The sections were first warmed to 56°C in a vacuum incubator (Isotemp Vacuum Oven, Thermo Fisher Scientific), then washed immediately twice in xylene, gradually redehydrated in ethanol (100, 95, and 70%, water), and then processed for antigen retrieval by microwave heating (1000 W, 6 min) in citrate buffer (10 mM, pH 6.0). Samples were then washed with phosphate-buffered saline (PBS), blocked with 1% bovine serum albumin (BSA)/5% donkey serum (1 hour, room temperature), and then incubated overnight at 4°C with primary antibodies (diluted in 0.5% BSA per the manufacturer's recommendation). The following day, samples were washed three times with PBS and incubated with appropriate fluorescent-labeled secondary antibodies (1:1000 dilution in 0.5% BSA, Life Technologies Inc.) and the nuclear marker DAPI (BioLegend). Slides were mounted using Gelvatol (Sigma-Aldrich) solution before imaging. Initial imaging was carried out using a 40×/1.3 numerical aperture (NA) objective lens on a Nikon Eclipse Ti Confocal microscope (Nikon, Melville, NY). Pixel sizes were 0.15 μm and *z* step size of 5 μm. High-resolution imaging was then conducted on the identical slides with a FluoView 1000 (Olympus Waltham, MA) using a 40×/1.30 NA objective lens. Antibodies used for mouse lung immunostaining are listed below.

Human TMA samples underwent deparaffination, washing, and gradual redehydration in a same manner as for processing mouse lung samples. Immunofluorescent staining was performed as described above for mouse lung samples. Human TMA samples were imaged on a wide-field RareCyte CyteFinder slide scanner with a 20×/0.75 NA objective lens with a pixel size of 0.65 μm per pixel. The excitation and emission filters were DAPI (excitation, 395/25; emission, 438/26), fluorescein isothiocyanate (excitation, 485/25; emission, 522/20), Cy3 (excitation, 555/20; emission, 590/20), and Cy5 (excitation, 651/11; emission, 692/44). Exposure times were adjusted to maximize dynamic range and eliminate saturation. High-resolution representative images from selected cores were acquired using a Zeiss LSM 880 confocal microscope.

Immunofluorescence antibodies: Please see table S4 for antibodies utilized in these studies.

Image quantification

For quantification of immunofluorescence images of mouse samples, image datasets were saved as .nd2 files and analyzed as maximum intensity projections since tissue samples had a thickness of one cell layer. Cells were segmented into individual objects based on the DAPI channel. Because of the fact that nuclei boundaries are ambiguous and hard to identify in tissue, we applied a preprocessing semantic segmentation step using a UNet model (*70*) trained on hand annotated DAPI-stained mouse and human tissue (https://github.com/HMS-IDAC/UnMicst). The architecture of the implemented model was similar to Saka *et al.* (*71*). Briefly, the model was trained to recognize and generate probability maps for nuclei contours, nuclei centers, and background pixels. CellProfiler (*72*) was then used to further segment nuclei based on the nuclei center probability maps made by the UNet model.

In CellProfiler, nuclei were identified using the Identify Primary Objects module where clumped cells were identified on the basis of shape. Next, the corresponding whole-cell region was obtained using the Identify Secondary Objects and dilating by 4 pixels since a common cytoplasm channel was absent from the experiment. The cytoplasmic regions were then obtained using Identify Tertiary Objects. Before acquiring measurements, the green, red, and Cy5 channels were background-subtracted by sampling the background intensities in the lower quartile range. The background-subtracted median intensities were then measured on a per-cell basis and exported to a csv file separated by nuclei, cytoplasm, and cell mask regions with entire cell mask region being used for further analysis. Segmentation mask overlays were also saved and inspected to evaluate the quality of segmentation. Image quantification values were reported as background-subtracted median ACE2 intensities in either all cells ($DAPI^+$) or in cells positive (above background) for indicated markers.

For quantification of the human TMA samples, images were acquired as separate overlapping tiles from a slide scanner. These tiles were stitched using ASHLAR, a novel stitching and registration algorithm (https://github.com/labsyspharm/ashlar) (*73*). Other custom scripts were used to systematically separate the stitched image into organized individual tissue cores (Coreograph; https://github.com/HMS-IDAC/UNetCoreograph), preprocess the image to identify cells, and suppress artifacts based on the DAPI channel (UnMicst; https://github.com/HMS-IDAC/UnMicst) (*74*) and segment cells into individual objects (S3segmenter; https://github.com/HMS-IDAC/S3segmenter). Upon closer inspection, we noticed that the staining quality of DAPI on the tissue cores was variable despite staining all cores under the same conditions. It is known that DNA deteriorates with age of sample causing lower binding of DAPI. This causes the signal-to-background ratio to be low where the nuclei are obfuscated by tissue autofluorescence and lastly leading to poor nuclei segmentation. We therefore inspected each core and only retained cores that had prominent DAPI staining above background. From these remaining cores, background-subtracted mean and median intensity measurements were obtained on a single-cell basis and exported to a csv file. Because running a large number of cores manually would be tedious, prone to errors, and require significant computational resources, all processes (stitching, core separation, preprocessing, single-cell segmentation, and quantification) were incorporated into a unified automated pipeline (mcmicro; https://github.com/labsyspharm/mcmicro) (*75*) that processed all samples in parallel on a high performance cluster. The background-subtracted median intensities were then measured on a per-cell basis and exported to a csv file separated by nuclei, cytoplasm, and cell mask regions with entire cell mask being used for further analysis. Cores containing fewer than 100 cells of a given type were excluded from analysis. Segmentation mask overlays were also saved and inspected to evaluate the quality of segmentation. Image quantification values were reported as background-subtracted ACE2 median intensities in either all cells ($DAPI^+$) or in cells positive (above background) for indicated markers.

Statistical analysis

The plotted data for ACE2 positivity are logit-transformed percent positive values, $Y_i = \log(p_i/(1 - p_i))$, where p_i is percent positive for subject i. To measure intraindividual heterogeneity, median absolute deviation was calculated on the basis of the log-transformed ACE2 signal intensities of all measured cells in each core. To test for association of this measure with age, a permutation test was used on the basis of Spearman's rank correlation. None of the three cell subsets (DAPI, PDPN, and AQP3) yielded a test result that indicated significant association (the P values were 0.871, 0.747, and 0.197, respectively). The observed Spearman correlations were 0.0187, −0.0378, and 0.194 for DAPI, PDPN, and AQP3, respectively.

To measure interindividual heterogeneity, cores were binned by age with a median ACE2 positivity calculated for each core. Weighted mean and SD of these median values were calculated for each bin.

BH3 profiling

Lung samples from mice of different ages (P0 to P62) were dissociated into a single-cell suspension using the Papain Dissociation System (Worthington Biochemical Corporation) with a modified protocol. Briefly, 50 to 100 g of lung samples were roughly chopped and submerged in 500 µl of Earle's Balanced Salt Solution (EBSS) with papain (20 U/ml) and 0.005% deoxyribonuclease (DNase) and incubated at 37°C with frequent agitation for 15 min. Samples were placed on ice and triturated with cut 1 ml pipette and were left to settle for 2 to 5 min before the cloudy cell suspension was transferred to new tubes and centrifuged at 200*g* for 5 min at 4°C. The resulting pellet was resuspended in EBSS with 0.005% DNase, BSA (1 mg/ml) and ovomucoid protease inhibitor (1 mg/ml). This suspension was layered on top of a solution of EBSS with BSA (10 mg/ml) and ovomucoid protease inhibitor (10 mg/ml) to create a discontinuous density gradient and then centrifuged at 72*g* for 6 min at room temperature. The supernatant was discarded and the pellet was resuspended in 100 µl of fluorescence-activated cell sorting (FACS) stain buffer [2% fetal bovine serum (FBS) in PBS] with 1 µl of anti–CD45-APC/Cy7 (allophycocyanin)/cyanine7 (clone 30-F11, BioLegend) and 1 µl of anti–EPCAM–Alexa Fluor 488 (clone G8.8, BioLegend).

Cells were stained on ice for 25 min away from light, then centrifuged at 200*g* for 5 min, and subjected to flow cytometry–based BH3 profiling as previously described (*40*). Briefly, cells were treated with activator or sensitizer BH3 peptides (New England Peptide) for 60 min at 28°C in mannitol experimental buffer (MEB) [10 mM Hepes (pH 7.5), 150 mM mannitol, 50 mM KCl, 0.02 mM EGTA, 0.02 mM EDTA, 0.1% BSA, and 5 mM succinate] with 0.001% digitonin. Peptide sequences are as follows: BIM (Ac-MRPEIWIAQELRRIGDEFNA-NH2), BID (Ac-EDIIRNIARHLAQVGDSMDRY-NH2), PUMA (p53 upregulated modulator of apoptosis) (Ac-EQWAREIGAQLRRMADDLNA-NH2), BAD (Ac-LWAAQRYGRELRRMSDEFEGSFKGL-NH2), Hrk (Harakiri) (Ac-WSSAAQLTAARLKALGDELHQ-NH2), and MS1 (MCL-1 specific) (Ac-RPEIWMTQGLRRLGDEINAYYAR-NH2). After peptide exposure,

cells were fixed in 2% PFA for 15 min which was then neutralized by addition of N_2 buffer [1.7 M tris base and 1.25 M glycine (pH 9.1)]. Cells were stained overnight with DAPI (1:1000, Abcam) and anti–cytochrome c–Alexa Fluor 647 (1:2000, clone 6H2.B4, BioLegend) in a saponin-based buffer (final concentration, 0.1% saponin; 1% BSA) and then analyzed by flow cytometry. Cytochrome c release in response to BIM treatment was measured on an Attune NxT flow cytometer (Thermo Fisher Scientific). Data for $EPCAM^+$ lung epithelial cells were collected from the $DAPI^+/CD45^-$ population.

Bortezomib treatment and measurement of apoptosis

To test the effect of bortezomib treatment on mouse lung cell apoptosis in vivo, young (P15 to P25) and old (P60 and older) mice were injected intraperitoneally with bortezomib dissolved in dimethyl sulfoxide (DMSO) at a dose of 2.5 mg/kg. After 24 hours, mice were euthanized and lung tissue was collected for analysis. Lung tissue was dissociated using papain as described for BH3 profiling experiments above. Dissociated cells were stained with EPCAM to mark epithelial cells and CellEvent Caspase-3/7 Green or DAPI to quantify apoptosis and cell death, respectively. Staining was assessed via flow cytometry with an Attune NxT cytometer.

ALI culture

Primary HTBE cells were obtained from American Type Culture Collection (ATCC) as described in fig. S7. Cells were thawed, cultured, and expanded according to supplier protocols in Airway Epithelial Cell Basal Medium (ATCC, #PCS300030) supplemented with Bronchial Epithelial Growth Kit reagents (ATCC, #PCS300040). After expanding for two passages, cells were frozen in complete medium supplemented with 10% FBS and 10% DMSO and stored in liquid nitrogen for subsequent use. To generate ALI cultures, primary cells at passage 3 were plated on six transwell inserts (Corning, #3460) per donor in a 12-well plate as described previously (*76*). Vials of cells were thawed and seeded in transwells in 50% bronchial epithelial cell growth basal medium (BEBM)/ 50% Dulbecco's modified Eagle's medium (DMEM) at a density of 76,000 cells/cm^2. Growth was monitored over 7 days until confluence, and on day 7 of culture, media was removed from the apical side of the transwell to establish an ALI. Cells were cultured for an additional 14 days to allow differentiation into cell types of interest.

On day 14 of ALI culture, well-differentiated cells from transwell inserts were harvested for BH3 profiling. To dissociate cells from the transwell insert membrane, cells were first washed with HBSS, then trypsin was added, and dissociation was carried out in a tissue culture incubator at 37°C. Periodically, trypsinized cells were aspirated and transferred to a Falcon tube containing culture media, and trypsin was refreshed to continue dissociation of remaining cells. The process was repeated until all cells were dissociated and collected in the Falcon tube. Cells were centrifuged and resuspended in 100 µl of FACS stain buffer with 1 µl of anti–EPCAM–Alexa Fluor 488 (BioLegend, #324210). Staining was carried out for 20 min on ice, and then cells were centrifuged and resuspended in MEB buffer for BH3 profiling as described above.

Chemosensitivity assays

To measure the induction of cell death by drug treatment, BEAS-2B or HTBE cells were seeded in 96-well plates in appropriate culture media. For BEAS-2B cells, plates were prepared in advance by coating with a solution of bovine collagen I (0.03 mg/ml; Sigma-Aldrich, #804592) in 0.02 N of acetic acid for 1 hour at room temperature and then by rinsing with PBS. Cells were seeded at a density of 5000 cells per well. The day after seeding, seeding media was removed and replaced with media containing indicated doses of bortezomib, BH3 mimetics, or DMSO vehicle control. Drug treatment was carried out for 48 hours, and then cells were trypsinized for staining and FACS analysis. To stain for markers of apoptosis, Alexa Fluor 488–conjugated annexin V (0.5 µg/ml; gift from T. Letai) and PI (1 µg/m; Thermo Fisher Scientific, #BMS500PI) were added to 10X annexin V binding buffer [0.1 M Hepes (pH 7.4), 1.4 M NaCl, and 25 mM CaCl2 solution, sterile filtered]. Ten microliters of 10X annexin/PI solution was added to 100 µl of cell suspension, and the mixture was incubated on ice away from light for 20 min. After staining, cells were analyzed immediately by flow cytometry using an Attune NxT cytometer.

Virus-induced cell death

SARS-CoV-2–triggered cell death of Vero E6 cells was monitored using an Incucyte S3. Virus was added to Vero E6 cells at multiplicity of infection (MOI) of 1 for 1 hour in DMEM/10% FBS at 37°C/5%CO_2, and then BH3 mimetics added for up to 48 hours. Cell viability was monitored using PI (1 µg/ml) on an Incucyte S3. Five fields of view at ×10 magnification representing 33.6% well coverage were monitored for changes in cell viability every 6 hours. PI-positive cells were identified using Incucyte software. All work with SARS-CoV-2 was conducted in BSL3 conditions at the UCSD following the guidelines approved by the Institutional Biosafety Committees.

SUPPLEMENTARY MATERIALS

Supplementary material for this article is available at http://advances.sciencemag.org/cgi/content/full/7/34/eabf8609/DC1

View/request a protocol for this paper from *Bio-protocol*.

REFERENCES AND NOTES

1. WHO, Situation reports (2020); www.who.int/emergencies/diseases/novel-coronavirus-2019/situation-reports.
2. CDC COVID-19 Response Team, Coronavirus disease 2019 in children—United States, February 12–April 2, 2020. *MMWR Morb. Mortal. Wkly Rep.* **69**, 422–426 (2020).
3. Y. Dong, X. Mo, Y. Hu, X. Qi, F. Jiang, Z. Jiang, S. Tong, Epidemiology of COVID-19 among children in China. *Pediatrics* **145**, e20200702 (2020).
4. N. Zhu, D. Zhang, W. Wang, X. Li, B. Yang, J. Song, X. Zhao, B. Huang, W. Shi, R. Lu, P. Niu, F. Zhan, X. Ma, D. Wang, W. Xu, G. Wu, G. F. Gao, W. Tan; China Novel Coronavirus Investigating and Research Team, A novel coronavirus from patients with pneumonia in China, 2019. *N. Engl. J. Med.* **382**, 727–733 (2020).
5. M. Hoffmann, H. Kleine-Weber, S. Schroeder, N. Krüger, T. Herrler, S. Erichsen, T. S. Schiergens, G. Herrler, N.-H. Wu, A. Nitsche, M. A. Müller, C. Drosten, S. Pöhlmann, SARS-CoV-2 cell entry depends on ACE2 and TMPRSS2 and is blocked by a clinically proven protease inhibitor. *Cell* **181**, 271–280.e8 (2020).
6. B. Treutlein, D. G. Brownfield, A. R. Wu, N. F. Neff, G. L. Mantalas, F. H. Espinoza, T. J. Desai, M. A. Krasnow, S. R. Quake, Reconstructing lineage hierarchies of the distal lung epithelium using single-cell RNA-seq. *Nature* **509**, 371–375 (2014).
7. H. Jia, Pulmonary angiotensin-converting enzyme 2 (ACE2) and inflammatory lung disease. *Shock* **46**, 239–248 (2016).
8. J. C. Smith, E. L. Sausville, V. Girish, M. L. Yuan, A. Vasudevan, K. M. John, J. M. Sheltzer, Cigarette smoke exposure and inflammatory signaling increase the expression of the SARS-CoV-2 receptor ACE2 in the respiratory tract. *Dev. Cell* **53**, 514–529.e3 (2020).
9. Y. Zhao, Z. Zhao, Y. Wang, Y. Zhou, Y. Ma, W. Zuo, Single-cell RNA expression profiling of ACE2, the receptor of SARS-CoV-2. *Am. J. Respir. Crit. Care Med.* **202**, 756–759 (2020).
10. K. J. Travaglini, A. N. Nabhan, L. Penland, R. Sinha, A. Gillich, R. V. Sit, S. Chang, S. D. Conley, Y. Mori, J. Seita, G. J. Berry, J. B. Shrager, R. J. Metzger, C. S. Kuo, N. Neff, I. L. Weissman, S. R. Quake, M. A. Krasnow, A molecular cell atlas of the human lung from single-cell RNA sequencing. *Nature* **587**, 619–625 (2020).
11. C. G. K. Ziegler, S. J. Allon, S. K. Nyquist, I. M. Mbano, V. N. Miao, C. N. Tzouanas, Y. Cao, A. S. Yousif, J. Bals, B. M. Hauser, J. Feldman, C. Muus, M. H. Wadsworth II, S. W. Kazer,

T. K. Hughes, B. Doran, G. J. Gatter, M. Vukovic, F. Taliaferro, B. E. Mead, Z. Guo, J. P. Wang, D. Gras, M. Plaisant, M. Ansari, I. Angelidis, H. Adler, J. M. S. Sucre, C. J. Taylor, B. Lin, A. Waghray, V. Mitsialis, D. F. Dwyer, K. M. Buchheit, J. A. Boyce, N. A. Barrett, T. M. Laidlaw, S. L. Carroll, L. Colonna, V. Tkachev, C. W. Peterson, A. Yu, H. B. Zheng, H. P. Gideon, C. G. Winchell, P. L. Lin, C. D. Bingle, S. B. Snapper, J. A. Kropski, F. J. Theis, H. B. Schiller, L.-E. Zaragosi, P. Barbry, A. Leslie, H.-P. Kiem, J. A. L. Flynn, S. M. Fortune, B. Berger, R. W. Finberg, L. S. Kean, M. Garber, A. G. Schmidt, D. Lingwood, A. K. Shalek, J. Ordovas-Montanes; HCA Lung Biological Network, SARS-CoV-2 receptor ACE2 is an interferon-stimulated gene in human airway epithelial cells and is detected in specific cell subsets across tissues. *Cell* **181**, 1016–1035.e19 (2020).

12. P. Danthi, Viruses and the diversity of cell death. *Annu. Rev. Virol.* **3**, 533–553 (2016).
13. M. H. Orzalli, J. C. Kagan, Apoptosis and necroptosis as host defense strategies to prevent viral infection. *Trends Cell Biol.* **27**, 800–809 (2017).
14. T. S. Fung, D. X. Liu, Coronavirus infection, ER stress, apoptosis and innate immunity. *Front. Microbiol.* **5**, 296 (2014).
15. X. Deng, M. Hackbart, R. C. Mettelman, A. O'Brien, A. M. Mielech, G. Yi, C. C. Kao, S. C. Baker, Coronavirus nonstructural protein 15 mediates evasion of dsRNA sensors and limits apoptosis in macrophages. *Proc. Natl. Acad. Sci. U.S.A.* **114**, E4251–E4260 (2017).
16. M. L. DeDiego, J. L. Nieto-Torres, J. M. Jiménez-Guardeño, J. A. Regla-Nava, E. Álvarez, J. C. Oliveros, J. Zhao, C. Fett, S. Perlman, L. Enjuanes, Severe acute respiratory syndrome coronavirus envelope protein regulates cell stress response and apoptosis. *PLOS Pathog.* **7**, e1002315 (2011).
17. Y.-J. Tan, S. G. Lim, W. Hong, Regulation of cell death during infection by the severe acute respiratory syndrome coronavirus and other coronaviruses. *Cell. Microbiol.* **9**, 2552–2561 (2007).
18. R. Singh, A. Letai, K. Sarosiek, Regulation of apoptosis in health and disease: The balancing act of BCL-2 family proteins. *Nat. Rev. Mol. Cell Biol.* **20**, 175–193 (2019).
19. K. A. Sarosiek, C. Fraser, N. Muthalagu, P. D. Bhola, W. Chang, S. K. McBrayer, A. Cantlon, S. Fisch, G. Golomb-Mello, J. A. Ryan, J. Deng, B. Jian, C. Corbett, M. Goldenberg, J. R. Madsen, R. Liao, D. Walsh, J. Sedivy, D. J. Murphy, D. R. Carrasco, S. Robinson, J. Moslehi, A. Letai, Developmental regulation of mitochondrial apoptosis by c-Myc governs age- and tissue-specific sensitivity to cancer therapeutics. *Cancer Cell* **31**, 142–156 (2017).
20. H. Pan, G. H. Deutsch, S. E. Wert; Ontology Subcommittee; NHLBI Molecular Atlas of Lung Development Program Consortium, Comprehensive anatomic ontologies for lung development: A comparison of alveolar formation and maturation within mouse and human lung. *J. Biomed. Semantics* **10**, 18 (2019).
21. H.-W. Snoeck, Modeling human lung development and disease using pluripotent stem cells. *Development* **142**, 13–16 (2015).
22. J. C. Schittny, Development of the lung. *Cell Tissue Res.* **367**, 427–444 (2017).
23. L. M. Gretebeck, K. Subbarao, Animal models for SARS and MERS coronaviruses. *Curr. Opin. Virol.* **13**, 123–129 (2015).
24. K. H. Dinnon III, S. R. Leist, A. Schäfer, C. E. Edwards, D. R. Martinez, S. A. Montgomery, A. West, B. L. Yount Jr., Y. J. Hou, L. E. Adams, K. L. Gully, A. J. Brown, E. Huang, M. D. Bryant, I. C. Choong, J. S. Glenn, L. E. Gralinski, T. P. Sheahan, R. S. Baric, A mouse-adapted model of SARS-CoV-2 to test COVID-19 countermeasures. *Nature* **586**, 560–566 (2020).
25. X. Montagutelli, M. Prot, L. Levillayer, E. B. Salazar, G. Jouvion, L. Conquet, F. Donati, M. Albert, F. Gambaro, S. Behillil, V. Enouf, D. Rousset, J. Jaubert, F. Rey, S. van der Werf, E. Simon-Loriere, The B1.351 and P.1 variants extend SARS-CoV-2 host range to mice. *bioRxiv*, 2021.03.18.436013 (2021).
26. T. Hruz, O. Laule, G. Szabo, F. Wessendorp, S. Bleuler, L. Oertle, P. Widmayer, W. Gruissem, P. Zimmermann, Genevestigator V3: A reference expression database for the meta-analysis of transcriptomes. *Adv. Bioinformatics* **2008**, 420747 (2008).
27. Y. Saini, H. Dang, A. Livraghi-Butrico, E. J. Kelly, L. C. Jones, W. K. O'Neal, R. C. Boucher, Gene expression in whole lung and pulmonary macrophages reflects the dynamic pathology associated with airway surface dehydration. *BMC Genomics* **15**, 726 (2014).
28. H.-Y. Cho, B. van Houten, X. Wang, L. Miller-DeGraff, J. Fostel, W. Gladwell, L. Perrow, V. Panduri, L. Kobzik, M. Yamamoto, D. A. Bell, S. R. Kleeberger, Targeted deletion of Nrf2 impairs lung development and oxidant injury in neonatal mice. *Antioxidants Redox Signal.* **17**, 1066–1082 (2012).
29. S. Srisuma, S. Bhattacharya, D. M. Simon, S. K. Solleti, S. Tyagi, B. Starcher, T. J. Mariani, Fibroblast growth factor receptors control epithelial-mesenchymal interactions necessary for alveolar elastogenesis. *Am. J. Respir. Crit. Care Med.* **181**, 838–850 (2010).
30. Y. Du, J. A. Kitzmiller, A. Sridharan, A. K. Perl, J. P. Bridges, R. S. Misra, G. S. Pryhuber, T. J. Mariani, S. Bhattacharya, M. Guo, S. S. Potter, P. Dexheimer, B. Aronow, A. H. Jobe, J. A. Whitsett, Y. Xu, Lung Gene Expression Analysis (LGEA): An integrative web portal for comprehensive gene expression data analysis in lung development. *Thorax* **72**, 481–484 (2017).
31. M. E. Ardini-Poleske, R. F. Clark, C. Ansong, J. P. Carson, R. A. Corley, G. H. Deutsch, J. S. Hagood, N. Kaminski, T. J. Mariani, S. S. Potter, G. S. Pryhuber, D. Warburton, J. A. Whitsett, S. M. Palmer, N. Ambalavanan; LungMAP Consortium, LungMAP: The molecular atlas of lung development program. *Am. J. Physiol. Lung Cell. Mol. Physiol.* **313**, L733–L740 (2017).
32. K. B. Engel, H. M. Moore, Effects of preanalytical variables on the detection of proteins by immunohistochemistry in formalin-fixed, paraffin-embedded tissue. *Arch. Pathol. Lab. Med.* **135**, 537–543 (2011).
33. B. T. Gaudette, N. N. Iwakoshi, L. H. Boise, Bcl-x_L protein protects from C/EBP homologous protein (CHOP)-dependent apoptosis during plasma cell differentiation. *J. Biol. Chem.* **289**, 23629–23640 (2014).
34. K. A. Sarosiek, L. E. Cavallin, S. Bhatt, N. L. Toomey, Y. Natkunam, W. Blasini, A. J. Gentles, J. C. Ramos, E. A. Mesri, I. S. Lossos, Efficacy of bortezomib in a direct xenograft model of primary effusion lymphoma. *Proc. Natl. Acad. Sci. U.S.A.* **107**, 13069–13074 (2010).
35. D. Blanco-Melo, B. E. Nilsson-Payant, W.-C. Liu, S. Uhl, D. Hoagland, R. Møller, T. X. Jordan, K. Oishi, M. Panis, D. Sachs, T. T. Wang, R. E. Schwartz, J. K. Lim, R. A. Albrecht, B. R. tenOever, Imbalanced host response to SARS-CoV-2 drives development of COVID-19. *Cell* **181**, 1036–1045.e9 (2020).
36. F. M. Wensveen, K. P. J. M. van Gisbergen, I. A. M. Derks, C. Gerlach, T. N. Schumacher, R. A. W. van Lier, E. Eldering, Apoptosis threshold set by noxa and Mcl-1 after T cell activation regulates competitive selection of high-affinity clones. *Immunity* **32**, 754–765 (2010).
37. M. D. Haschka, C. Soratroi, S. Kirschnek, G. Häcker, R. Hilbe, S. Geley, A. Villunger, L. L. Fava, The NOXA–MCL1–BIM axis defines lifespan on extended mitotic arrest. *Nat. Commun.* **6**, 6891 (2015).
38. L. Chen, S. N. Willis, A. Wei, B. J. Smith, J. I. Fletcher, M. G. Hinds, P. M. Colman, C. L. Day, J. M. Adams, D. C. S. Huang, Differential targeting of prosurvival Bcl-2 proteins by their BH3-only ligands allows complementary apoptotic function. *Mol. Cell* **17**, 393–403 (2005).
39. C. Fraser, A. Presser, V. Sanchorawala, S. Sarosiek, K. Sarosiek, Clonal plasma cells in AL amyloidosis are dependent on pro survival BCL-2 family proteins and sensitive to BH3 mimetics. *bioRxiv* , 542159 (2019).
40. C. Fraser, J. Ryan, K. Sarosiek, BH3 profiling: A functional assay to measure apoptotic priming and dependencies. *Methods Mol. Biol.* **1877**, 61–76 (2019).
41. N. Nikesitch, J. M. Lee, S. Ling, T. L. Roberts, Endoplasmic reticulum stress in the development of multiple myeloma and drug resistance. *Clin. Transl. Immunol.* **7**, e1007 (2018).
42. K. Austgen, S. A. Oakes, D. Ganem, Multiple defects, including premature apoptosis, prevent Kaposi's sarcoma-associated herpesvirus replication in murine cells. *J. Virol.* **86**, 1877–1882 (2012).
43. K. F. Hui, B. H. W. Lam, D. N. Ho, S. W. Tsao, A. K. S. Chiang, Bortezomib and SAHA synergistically induce ROS-driven caspase-dependent apoptosis of nasopharyngeal carcinoma and block replication of Epstein–Barr virus. *Mol. Cancer Ther.* **12**, 747–758 (2013).
44. K. A. Sarosiek, A. Letai, Directly targeting the mitochondrial pathway of apoptosis for cancer therapy using BH3 mimetics - recent successes, current challenges and future promise. *FEBS J.* **283**, 3523–3533 (2016).
45. D. Merino, G. L. Kelly, G. Lessene, A. H. Wei, A. W. Roberts, A. Strasser, BH3-mimetic drugs: Blazing the trail for new cancer medicines. *Cancer Cell* **34**, 879–891 (2018).
46. S. E. Fox, A. Akmatbekov, J. L. Harbert, G. Li, J. Q. Brown, R. S. Vander Heide, Pulmonary and cardiac pathology in African American patients with COVID-19: An autopsy series from New Orleans. *Lancet Respir. Med.* **8**, 10.1016/S2213-2600(20)30243-5 (2020).
47. C. Wu, M. Zheng, Single-cell RNA expression profiling shows that ACE2, the putative receptor of Wuhan 2019-nCoV, has significant expression in the nasal, mouth, lung and colon tissues, and tends to be co-expressed with HLA-DRB1 in the four tissues (Preprints, 2020); www.preprints.org.
48. A. Gupta, M. V. Madhavan, K. Sehgal, N. Nair, S. Mahajan, T. S. Sehrawat, B. Bikdeli, N. Ahluwalia, J. C. Ausiello, E. Y. Wan, D. E. Freedberg, A. J. Kirtane, S. A. Parikh, M. S. Maurer, A. S. Nordvig, D. Accili, J. M. Bathon, S. Mohan, K. A. Bauer, M. B. Leon, H. M. Krumholz, N. Uriel, M. R. Mehra, M. S. V. Elkind, G. W. Stone, A. Schwartz, D. D. Ho, J. P. Bilezikian, D. W. Landry, Extrapulmonary manifestations of COVID-19. *Nat. Med.* **26**, 1017–1032 (2020).
49. M.-S. Kim, S. M. Pinto, D. Getnet, R. S. Nirujogi, S. S. Manda, R. Chaerkady, A. K. Madugundu, D. S. Kelkar, R. Isserlin, S. Jain, J. K. Thomas, B. Muthusamy, P. Leal-Rojas, P. Kumar, N. A. Sahasrabuddhe, L. Balakrishnan, J. Advani, B. George, S. Renuse, L. D. N. Selvan, A. H. Patil, V. Nanjappa, A. Radhakrishnan, S. Prasad, T. Subbannayya, R. Raju, M. Kumar, S. K. Sreenivasamurthy, A. Marimuthu, G. J. Sathe, S. Chavan, K. K. Datta, Y. Subbannayya, A. Sahu, S. D. Yelamanchi, S. Jayaram, P. Rajagopalan, J. Sharma, K. R. Murthy, N. Syed, R. Goel, A. a Khan, S. Ahmad, G. Dey, K. Mudgal, A. Chatterjee, T.-C. Huang, J. Zhong, X. Wu, P. G. Shaw, D. Freed, M. S. Zahari, K. K. Mukherjee, S. Shankar, A. Mahadevan, H. Lam, C. J. Mitchell, S. K. Shankar, P. Satishchandra, J. T. Schroeder, R. Sirdeshmukh, A. Maitra, S. D. Leach, C. G. Drake, M. K. Halushka, T. S. K. Prasad, R. H. Hruban, C. L. Kerr, G. D. Bader, C. A. Iacobuzio-Donahue,

H. Gowda, A. Pandey, A draft map of the human proteome. *Nature* **509**, 575–581 (2014).
50. M. Cardoso-Moreira, J. Halbert, D. Valloton, B. Velten, C. Chen, Y. Shao, A. Liechti, K. Ascenção, C. Rummel, S. Ovchinnikova, P. V. Mazin, I. Xenarios, K. Harshman, M. Mort, D. N. Cooper, C. Sandi, M. J. Soares, P. G. Ferreira, S. Afonso, M. Carneiro, J. M. A. Turner, J. L. VandeBerg, A. Fallahshahroudi, P. Jensen, R. Behr, S. Lisgo, S. Lindsay, P. Khaitovich, W. Huber, J. Baker, S. Anders, Y. E. Zhang, H. Kaessmann, Gene expression across mammalian organ development. *Nature* **571**, 505–509 (2019).
51. H. Qiu, J. Wu, L. Hong, Y. Luo, Q. Song, D. Chen, Clinical and epidemiological features of 36 children with coronavirus disease 2019 (COVID-19) in Zhejiang, China: An observational cohort study. *Lancet Infect. Dis.* **20**, 689–696 (2020).
52. Y. Cui, M. Tian, D. Huang, X. Wang, Y. Huang, L. Fan, L. Wang, Y. Chen, W. Liu, K. Zhang, Y. Wu, Z. Yang, J. Tao, J. Feng, K. Liu, X. Ye, R. Wang, X. Zhang, Y. Zha, A 55-day-old female infant infected with 2019 novel coronavirus disease: Presenting with pneumonia, liver injury, and heart damage. *J. Infect. Dis.* **221**, 1775–1781 (2020).
53. M. Madjid, P. Safavi-Naeini, S. D. Solomon, O. Vardeny, Potential effects of coronaviruses on the cardiovascular system: A review. *JAMA Cardiol.* **5**, 831–840 (2020).
54. E. M. Abrams, S. J. Szefler, COVID-19 and the impact of social determinants of health. *Lancet Respir. Med.* **8**, 659–661 (2020).
55. T. Oltersdorf, S. W. Elmore, A. R. Shoemaker, R. C. Armstrong, D. J. Augeri, B. A. Belli, M. Bruncko, T. L. Deckwerth, J. Dinges, P. J. Hajduk, M. K. Joseph, S. Kitada, S. J. Korsmeyer, A. R. Kunzer, A. Letai, C. Li, M. J. Mitten, D. G. Nettesheim, S. Ng, P. M. Nimmer, J. M. O'Connor, A. Oleksijew, A. M. Petros, J. C. Reed, W. Shen, S. K. Tahir, C. B. Thompson, K. J. Tomaselli, B. Wang, M. D. Wendt, H. Zhang, S. W. Fesik, S. H. Rosenberg, An inhibitor of Bcl-2 family proteins induces regression of solid tumours. *Nature* **435**, 677–681 (2005).
56. A. Letai, Apoptosis and cancer. *Annu. Rev. Cancer Biol.* **1**, 275–294 (2017).
57. R. L. Schenk, A. Strasser, G. Dewson, BCL-2: Long and winding path from discovery to therapeutic target. *Biochem. Biophys. Res. Commun.* **482**, 459–469 (2017).
58. C. B. Medina, P. Mehrotra, S. Arandjelovic, J. S. A. Perry, Y. Guo, S. Morioka, B. Barron, S. F. Walk, B. Ghesquière, A. S. Krupnick, U. Lorenz, K. S. Ravichandran, Metabolites released from apoptotic cells act as tissue messengers. *Nature* **580**, 130–135 (2020).
59. L. Scarfò, T. Chatzikonstantinou, G. M. Rigolin, G. Quaresmini, M. Motta, C. Vitale, J. A. Garcia-Marco, J. Á. Hernández-Rivas, F. Mirás, M. Baile, J. Marquet, C. U. Niemann, G. Reda, T. Munir, E. Gimeno, M. Marchetti, F. M. Quaglia, M. Varettoni, J. Delgado, S. Iyengar, A. Janssens, R. Marasca, A. Ferrari, C. Cuéllar-García, G. Itchaki, M. Špaček, L. De Paoli, L. Laurenti, M. D. Levin, E. Lista, F. R. Mauro, M. Šimkovič, E. Van Der Spek, E. Vandenberghe, L. Trentin, E. Wasik-Szczepanek, R. Ruchlemer, D. Bron, M. R. De Paolis, G. Del Poeta, L. Farina, M. Foglietta, M. Gentile, Y. Herishanu, T. Herold, O. Jaksic, A. P. Kater, S. Kersting, L. Malerba, L. Orsucci, V. M. Popov, P. Sportoletti, M. Yassin, B. Pocali, G. Barna, A. Chiarenza, G. dos Santos, E. Nikitin, M. Andres, M. Dimou, M. Doubek, A. Enrico, Y. Hakobyan, O. Kalashnikova, M. Ortiz Pareja, M. Papaioannou, D. Rossi, N. Shah, A. Shrestha, O. Stanca, N. Stavroyianni, V. Strugov, C. Tam, M. Zdrenghea, M. Coscia, K. Stamatopoulos, G. Rossi, A. Rambaldi, E. Montserrat, R. Foà, A. Cuneo, P. Ghia, COVID-19 severity and mortality in patients with chronic lymphocytic leukemia: A joint study by ERIC, the European Research Initiative on CLL, and CLL Campus. *Leukemia* **34**, 2354–2363 (2020).
60. S. P. Treon, J. J. Castillo, A. P. Skarbnik, J. D. Soumerai, I. M. Ghobrial, M. L. Guerrera, K. Meid, G. Yang, The BTK inhibitor ibrutinib may protect against pulmonary injury in COVID-19-infected patients. *Blood* **135**, 1912–1915 (2020).
61. T. S. Fung, Y. Liao, D. X. Liu, The endoplasmic reticulum stress sensor IRE1α protects cells from apoptosis induced by the coronavirus infectious bronchitis virus. *J. Virol.* **88**, 12752–12764 (2014).
62. K. K.-W. To, O. T.-Y. Tsang, W.-S. Leung, A. R. Tam, T.-C. Wu, D. C. Lung, C. C.-Y. Yip, J.-P. Cai, J. M.-C. Chan, T. S.-H. Chik, D. P.-L. Lau, C. Y.-C. Choi, L.-L. Chen, W.-M. Chan, K.-H. Chan, J. D. Ip, A. C.-K. Ng, R. W.-S. Poon, C.-T. Luo, V. C.-C. Cheng, J. F.-W. Chan, I. F.-N. Hung, Z. Chen, H. Chen, K.-Y. Yuen, Temporal profiles of viral load in posterior oropharyngeal saliva samples and serum antibody responses during infection by SARS-CoV-2: An observational cohort study. *Lancet Infect. Dis.* **20**, 565–574 (2020).
63. F. M. K. Williams, M. B. Freydin, M. Mangino, S. Couvreur, A. Visconti, R. C. E. Bowyer, C. I. Le Roy, M. Falchi, O. Mompeó, C. Sudre, R. Davies, C. Hammond, C. Menni, C. J. Steves, T. D. Spector, Self-reported symptoms of COVID-19, including symptoms most predictive of SARS-CoV-2 infection, are heritable. *Twin Res. Hum. Genet.* **23**, 316–321 (2020).
64. RECOVERY Collaborative Group, Dexamethasone in hospitalized patients with Covid-19. *N. Engl. J. Med.* **384**, 693–704 (2021).
65. J. Hansen, A. Baum, K. E. Pascal, V. Russo, S. Giordano, E. Wloga, B. O. Fulton, Y. Yan, K. Koon, K. Patel, K. M. Chung, A. Hermann, E. Ullman, J. Cruz, A. Rafique, T. Huang, J. Fairhurst, C. Libertiny, M. Malbec, W. Lee, R. Welsh, G. Farr, S. Pennington, D. Deshpande, J. Cheng, A. Watty, P. Bouffard, R. Babb, N. Levenkova, C. Chen, B. Zhang, A. Romero Hernandez, K. Saotome, Y. Zhou, M. Franklin, S. Sivapalasingam, D. C. Lye, S. Weston, J. Logue, R. Haupt, M. Frieman, G. Chen, W. Olson, A. J. Murphy, N. Stahl, G. D. Yancopoulos, C. A. Kyratsous, Studies in humanized mice and convalescent humans yield a SARS-CoV-2 antibody cocktail. *Science* **369**, 1010–1014 (2020).
66. L. M. Burrell, C. I. Johnston, C. Tikellis, M. E. Cooper, ACE2, a new regulator of the renin–angiotensin system. *Trends Endocrinol. Metab.* **15**, 166–169 (2004).
67. M. Cohen, A. Giladi, A.-D. Gorki, D. G. Solodkin, M. Zada, A. Hladik, A. Miklosi, T.-M. Salame, K. B. Halpern, E. David, S. Itzkovitz, T. Harkany, S. Knapp, I. Amit, Lung single-cell signaling interaction map reveals basophil role in macrophage imprinting. *Cell* **175**, 1031–1044. e18 (2018).
68. P. A. Reyfman, J. M. Walter, N. Joshi, K. R. Anekalla, A. C. McQuattie-Pimentel, S. Chiu, R. Fernandez, M. Akbarpour, C. I. Chen, Z. Ren, R. Verma, H. Abdala-Valencia, K. Nam, M. Chi, S. H. Han, F. J. Gonzalez-Gonzalez, S. Soberanes, S. Watanabe, K. J. N. Williams, A. S. Flozak, T. T. Nicholson, V. K. Morgan, D. R. Winter, M. Hinchcliff, C. L. Hrusch, R. D. Guzy, C. A. Bonham, A. I. Sperling, R. Bag, R. B. Hamanaka, G. M. Mutlu, A. V. Yeldandi, S. A. Marshall, A. Shilatifard, L. A. N. Amaral, H. Perlman, J. I. Sznajder, A. Christine Argento, C. T. Gillespie, J. Dematte, M. Jain, B. D. Singer, K. M. Ridge, A. P. Lam, A. Bharat, S. M. Bhorade, C. J. Gottardi, G. R. Scott Budinger, A. V. Misharin, Single-cell transcriptomic analysis of human lung provides insights into the pathobiology of pulmonary fibrosis. *Am. J. Respir. Crit. Care Med.* **199**, 1517–1536 (2019).
69. T. Stuart, A. Butler, P. Hoffman, C. Hafemeister, E. Papalexi, W. M. Mauck III, Y. Hao, M. Stoeckius, P. Smibert, R. Satija, Comprehensive integration of single-cell data. *Cell* **177**, 1888–1902.e21 (2019).
70. O. Ronneberger, P. Fischer, T. Brox, in *Lecture Notes in Computer Science (including subseries Lecture Notes in Artificial Intelligence and Lecture Notes in Bioinformatics)* (Springer Verlag, 2015), vol. 9351, pp. 234–241.
71. S. K. Saka, Y. Wang, J. Y. Kishi, A. Zhu, Y. Zeng, W. Xie, K. Kirli, C. Yapp, M. Cicconet, B. J. Beliveau, S. W. Lapan, S. Yin, M. Lin, E. S. Boyden, P. S. Kaeser, G. Pihan, G. M. Church, P. Yin, Immuno-SABER enables highly multiplexed and amplified protein imaging in tissues. *Nat. Biotechnol.* **37**, 1080–1090 (2019).
72. C. McQuin, A. Goodman, V. Chernyshev, L. Kamentsky, B. A. Cimini, K. W. Karhohs, M. Doan, L. Ding, S. M. Rafelski, D. Thirstrup, W. Wiegraebe, S. Singh, T. Becker, J. C. Caicedo, A. E. Carpenter, CellProfiler 3.0: Next-generation image processing for biology. *PLOS Biol.* **16**, e2005970 (2018).
73. J. Muhlich, Y.-A. Chen, D. Russell, P. K. Sorger, Stitching and registering highly multiplexed whole slide images of tissues and tumors using ASHLAR software. *bioRxiv*, 2021.04.20.440625 (2021).
74. C. Yapp, E. Novikov, W.-D. Jang, Y.-A. Chen, M. Cicconet, Z. Maliga, C. A. Jacobson, D. Wei, S. Santagata, H. Pfister, P. K. Sorger, UnMICST: Deep learning with real augmentation for robust segmentation of highly multiplexed images of human tissues. *bioRxiv*, 2021.04.02.438285 (2021).
75. D. Schapiro, A. Sokolov, C. Yapp, J. L. Muhlich, J. Hess, J.-R. Lin, Y.-A. Chen, M. K. Nariya, G. J. Baker, J. Ruokonen, Z. Maliga, C. A. Jacobson, S. L. Farhi, D. Abbondanza, E. T. McKinley, C. Betts, A. Regev, R. J. Coffey, L. M. Coussens, S. Santagata, P. K. Sorger, MCMICRO: A scalable, modular image-processing pipeline for multiplexed tissue imaging. *bioRxiv*, 2021.03.15.435473 (2021).
76. M. J. O'Sullivan, J. A. Mitchel, C. Mwase, M. McGill, P. Kanki, J.-A. Park, In well-differentiated primary human bronchial epithelial cells, TGF-β1 and TGF-β2 induce expression of furin. *Am. J. Physiol. Lung Cell. Mol. Physiol.* **320**, L246–L253 (2021).
77. D. E. Wentworth, L. Gillim-Ross, N. Espina, K. A. Bernard, Mice susceptible to SARS coronavirus. *Emerg. Infect. Dis.* **10**, 1293–1296 (2004).
78. K. Subbarao, J. McAuliffe, L. Vogel, G. Fahle, S. Fischer, K. Tatti, M. Packard, W.-J. Shieh, S. Zaki, B. Murphy, Prior infection and passive transfer of neutralizing antibody prevent replication of severe acute respiratory syndrome coronavirus in the respiratory tract of mice. *J. Virol.* **78**, 3572–3577 (2004).
79. W. G. Glass, K. Subbarao, B. Murphy, P. M. Murphy, Mechanisms of host defense following severe acute respiratory syndrome-coronavirus (SARS-CoV) pulmonary infection of mice. *J. Immunol.* **173**, 4030–4039 (2004).
80. A. Roberts, D. Deming, C. D. Paddock, A. Cheng, B. Yount, L. Vogel, B. D. Herman, T. Sheahan, M. Heise, G. L. Genrich, S. R. Zaki, R. Baric, K. Subbarao, A mouse-adapted SARS-coronavirus causes disease and mortality in BALB/c mice. *PLOS Pathog.* **3**, e5 (2007).
81. T. Baas, A. Roberts, T. H. Teal, L. Vogel, J. Chen, T. M. Tumpey, M. G. Katze, K. Subbarao, Genomic analysis reveals age-dependent innate immune responses to severe acute respiratory syndrome coronavirus. *J. Virol.* **82**, 9465–9476 (2008).
82. C.-T. K. Tseng, C. Huang, P. Newman, N. Wang, K. Narayanan, D. M. Watts, S. Makino, M. M. Packard, S. R. Zaki, T.-s. Chan, C. J. Peters, Severe acute respiratory syndrome coronavirus infection of mice transgenic for the human angiotensin-converting enzyme 2 virus receptor. *J. Virol.* **81**, 1162–1173 (2007).
83. A. Roberts, C. Paddock, L. Vogel, E. Butler, S. Zaki, K. Subbarao, Aged BALB/c mice as a model for increased severity of severe acute respiratory syndrome in elderly humans. *J. Virol.* **79**, 5833–5838 (2005).

84. R. J. Hogan, G. Gao, T. Rowe, P. Bell, D. Flieder, J. Paragas, G. P. Kobinger, N. A. Wivel, R. G. Crystal, J. Boyer, H. Feldmann, T. G. Voss, J. M. Wilson, Resolution of primary severe acute respiratory syndrome-associated coronavirus infection requires Stat1. *J. Virol.* **78**, 11416–11421 (2004).
85. P. B. McCray Jr., L. Pewe, C. Wohlford-Lenane, M. Hickey, L. Manzel, L. Shi, J. Netland, H. P. Jia, C. Halabi, C. D. Sigmund, D. K. Meyerholz, P. Kirby, D. C. Look, S. Perlman, Lethal infection of K18-hACE2 mice infected with severe acute respiratory syndrome coronavirus. *J. Virol.* **81**, 813–821 (2007).

Acknowledgments: We thank the members of our labs for comments and suggestions on this work, especially K. Webster for assistance with image quantification. We thank O. Popow (Dana Farber Cancer Institute) for providing training data for the UNet model and Z. Maliga (Harvard Program in Therapeutic Science) for imaging the human TMA samples and advising on staining protocols. Imaging experiments were supported, in part, by the Emory University Integrated Cellular Imaging Microscopy Core. Some figures contain images sourced from Servier Medical Art (smart.servier.com). **Funding:** This work was supported by funding from the HSPH Dean's Fund for Scientific Advancement (to K.A.S.), the HSPH National Institute for Environmental Health Sciences (NIEHS) Center (K.A.S. and J.S.) (R00CA188679 to K.A.S., R01CA248565 to K.A.S., R37CA248565 to K.A.S., R01DK125263 to K.A.S., R21AI149321 to H.J., R01AI148446 to H.J., and 3R21AI149321-01S1 to H.J.), Harvard Center for Cancer Systems Pharmacology (U54CA225088 to C.Y., W911NF-19-2-0017 to C.Y., and RO1 HL124209 B.A.C.), the American Asthma Foundation (B.A.C.) (BSF 2017176 to B.A.C., K08 AI130381 to A.F.C., and R01 HL148152 to J.P.), COVID-19 Acceleration Award/Harvard T.H. Chan School of Public Health (P30ES000002 to J.P.), a career award from American Heart Association (20CDA35320302 to Y.P.Z.), and a Career Award for Medical Scientists from the Burroughs Welcome Fund (to A.F.C.). The following reagent was deposited by the Centers for Disease Control and Prevention and obtained through BEI resources, NIAID, NIH: SARS-Related Coronavirus 2, Isolate USA-WA1/2020, Heat Inactivated, NR-52286. The following reagent was deposited by the Centers for Disease Control and Prevention and obtained through BEI resources, NIAID, NIH: SARS-Related Coronavirus 2, Isolate USA-WA1/2020, NR-52281. We thank Sartorius for the use of the Incucyte S3 microscope system. **Author contributions:** K.A.S., B.A.C., and Z.I. conceived the study. Z.I., C.Y., B.A.C., S.L.L., B.D., E.G., D.B., and K.A.S. analyzed data. Z.I., B.D., H.J., G.N.J., B.A.C., S.L.L., L.X., X.S., J.C.L., and A.F.G., conducted imaging experiments. Z.I., J.S., and C.F. conducted BH3 profiling experiments. G.W. and J.-A.P. designed and conducted ALI culture experiments. B.A.C., A.E.C., S.L.L., A.F.C., Y.P.Z., and J.C.L. conducted live SARS-CoV-2 infection experiments. C.S., D.J.H., L.E.C.-A., J.M.D., V.P., A.F.C., C.L., A.N.H., and H.J. provided samples for analysis. L.K., X.S., L.X., and S.L.L. conducted pathological analysis of samples. Z.I. and K.A.S. wrote the manuscript. All authors edited and approved the final manuscript. **Competing interests:** The authors declare that they have no competing interests. **Data and materials availability:** All data needed to evaluate the conclusions in the paper are present in the paper and/or the Supplementary Materials. Raw images and other unprocessed data are available and will be shared by the authors upon request.

Submitted 24 November 2020
Accepted 25 June 2021
Published 18 August 2021
10.1126/sciadv.abf8609

Citation: Z. Inde, B. A. Croker, C. Yapp, G. N. Joshi, J. Spetz, C. Fraser, X. Qin, L. Xu, B. Deskin, E. Ghelfi, G. Webb, A. F. Carlin, Y. P. Zhu, S. L. Leibel, A. F. Garretson, A. E. Clark, J. M. Duran, V. Pretorius, L. E. Crotty-Alexander, C. Li, J. C. Lee, C. Sodhi, D. J. Hackam, X. Sun, A. N. Hata, L. Kobzik, J. Miller, J.-A. Park, D. Brownfield, H. Jia, K. A. Sarosiek, Age-dependent regulation of SARS-CoV-2 cell entry genes and cell death programs correlates with COVID-19 severity. *Sci. Adv.* **7**, eabf8609 (2021).